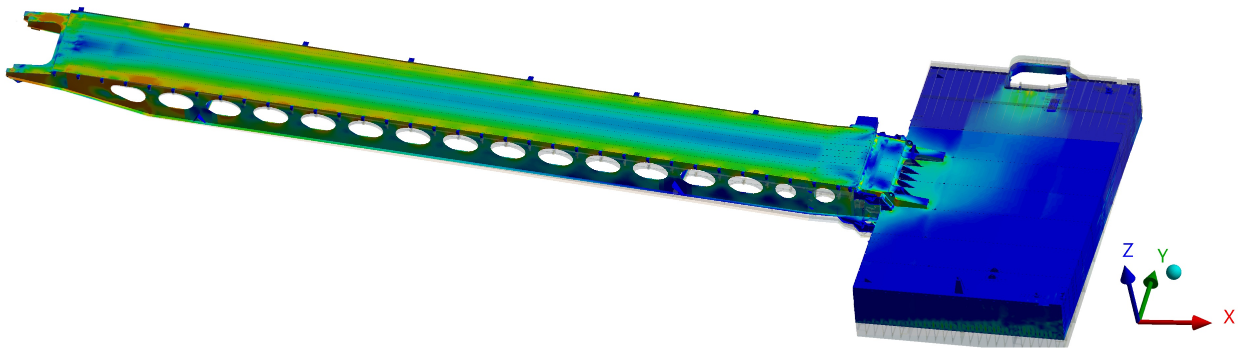

Hydrodynamic Behaviour of a Floating Linkspan

A Study on Wave Responses

Master's thesis in Applied Mechanics

YOUSEF AMIRI

POUYA SHEIKHOLESLAMI

Department of Mechanics and Maritime Sciences
CHALMERS UNIVERSITY OF TECHNOLOGY
Gothenburg, Sweden 2021
www.chalmers.se

Master's thesis 2021

Hydrodynamic Behaviour of a Floating Linkspan

A study on wave responses

YOUSEF AMIRI
POUYA SHEIKHOLESLAMI

Department of Mechanics and Maritime Sciences
Division of Marine Technology
Chalmers University of Technology
Gothenburg, Sweden 2021

Hydrodynamic Behaviour of a Floating Linkspan
A Study on Wave Responses
YOUSEF AMIRI
POUYA SHEIKHOLESLAMI

Supervisors at the company: Jonas Pedersen, MacGregor
David Engerberg, MacGregor
Kajsa Malm Gustafsson, MacGregor
Examiner: Wengang Mao, Mechanics and Maritime Sciences
Supervisor at Chalmers: Wengang Mao, Mechanics and Maritime Sciences

Master's Thesis 2021
Department of Mechanics and Maritime Sciences
Division of Marine Technology
Chalmers University of Technology
SE-412 96 Gothenburg
Telephone +46 31 772 1000

Cover: Equivalent(von-Mises) stress result at Lowest Astronomical Tide level, with pitch angle of 5.71° influenced by the peak period 90° regular wave.

Typeset in LaTeX
Printed by Chalmers Reproservice
Gothenburg, Sweden 2021

Hydrodynamic Behaviour of a Floating Linkspan
A Study on Wave Responses
YOUSEF AMIRI
POUYA SHEIKHOLESLAMI
Department of Mechanics and Maritime Sciences
Chalmers University of Technology

Abstract

Maritime transport is an important part of global trade. Ro-Ro transports standing for roll-on-roll-off is a an important part of maritime transport. Ro-Ro transports is closely related to the concept of linksapn. Tide and waves can make access to quay difficult. A linkspan, as a solution is a facility to provide a good connection between shore and ship for discharging and loading.

In this thesis firstly, a hydrodynamic study is performed on an integral tank linkspan to understand how environmental factors such as wave at extreme tide levels (Highest and Lowest Astronomical Tide) in combination with extreme loading conditions (Full and Empty) affect the motion of the linkspan. Secondly, a load mapping approach is performed to study the wave impacts from a structural strength perspective. This approach is based on using inertia information from the hydrodynamic or the structural model, since these are not the same. The feasibility of the load mapping approach is also assessed.

Heave and pitch motion is studied in head sea (180° wave heading angle) while roll motion is studied in beam sea (90° wave heading angle) in the hydrodynamic analysis. The results have shown that at small wave periods the pitch motion is unfavorable at the highest tide level. Maximum roll motion is obtained at smaller wavelength to structure length ratio in comparison to the heave motion.

The load mapping reflects the wave situation fairly good and the wave impact can be reflected in the deformation contour-plots. It is found that the maximum stress in the load mapping part is obtained at the hinges. It is also found that by using inertia from structural model a more realistic result in terms of deformation is obtained.

Keywords: potential flow, Source Distribution Method, Ansys Aqwa, Response Amplitude Operator, Finite Element Method, incident wave, diffraction wave, radiation Wave, wave spectra, heave, pitch, roll.

Acknowledgements

This project thesis was performed in a collaboration with MacGregor Sweden AB. It was presented during the defence of our MSc thesis on 4^{th} of June 2021 for 30 credits towards the international master's program in Naval Architecture and Ocean Engineering at Chalmers University of Technology.

We would like to thank our supervisors at MacGregor, David Engerberg and Kajsa Malm Gustafsson. Without your persistent support, the goal of this project would not have been realized. We would also like to thank Jonas Pedersen for offering us this possibility to carry out this interesting project at MacGregor.

We also wish to express our sincere gratitude to our supervisor and examiner at Chalmers, Professor Wengang Mao, for his practical suggestions during several stages of the thesis. Your inputs were truly valuable.

Lastly, we would like to extend our gratitude to our families and friend for continuously providing moral support.

Yousef Amiri and Pouya Sheikholeslami, Gothenburg, June 2021

Contents

List of Figures

List of Tables

Nomenclature

Upper-case Roman

$\boldsymbol{B}$	Hydrodynamic damping matrix
$\boldsymbol{C}$	Hydrostatic stiffness matrix
$\boldsymbol{A}$	Hydrodynamic added mass matrix
$\boldsymbol{F}$	Wave excitation force and moments
$\boldsymbol{F}_{dj}$	Diffraction wave force vector
$\boldsymbol{F}_{Ij}$	Incident wave force vector
$\boldsymbol{F}_{rjk}$	Radiation wave force matrix
$\Delta\boldsymbol{C}$	Additional hydrostatic stiffness matrix
$F(\gamma)$	Weighting function
H	Transfer function
H_s	Significant wave height
I_{xx}	Mass moment of inertia around x-axis
I_{yy}	Mass moment of inertia around y-axis
I_{zz}	Mass moment of inertia around z-axis
M_{xx}	Torsional moment around $x-$axis
M_{yy}	Torsional Moment around $y-$axis
S	Spectral Ordinate
S_0	Wetted surface
S_p	Average wave steepness
S_s	Significant wave steepness
T	Wave period
T_p	Peak period
T_z	Zero-up-crossing period

Lower-case Roman

$\boldsymbol{r}$	Position vector with respect to COG
a_i	Wave amplitude for a unique regular wave
a_w	Wave amplitude
d	Water depth
dt	Elapsed time since the wave crest passed structure COG
g	Gravitation constant
k_i	Wave number
k_{xx}	radius of gyration around x-axis
k_{yy}	radius of gyration around y-axis
k_{zz}	radius of gyration around z-axis
m	Mass
n_j	Unit normal
u	Velocity component in x-direction
v	Velocity component in y-direction
w	Velocity component in z-direction

Upper-case Greek

ω	Wave frequency
ω_p	Peak frequency

Lower-case Greek

α	Factor that depends on wind speed and peak factor
$\boldsymbol{\eta}$	Structural response vector
γt	Peck enhancement factor
ω_n	Last frequency
ω_p	Peak frequency of the spectrum
ϕ	Velocity potential
σ	spectral width parameter
θ_{xx}	Roll angle
θ_{yy}	Pitch angle
φ_i	Random phase angle
ζ	Wave surface elevation
Other	
∇	Gradient operator
Abbreviations	
APDL	ANSYS Parametric Design Language
CAD	Computer-Aided Design
CFD	Computational Fluid Dynamics
COG	Central Of Gravity
FE	Finite Element
HAT	Highest Astronomical Tide
JONSWAP	Joint North Sea Wave Observation Project
LAT	Lowest Astronomical Tide
RAO	Response Amplitude Operator
SFE	Specifies Surface loads on Elements

1
Introduction

Maritime transport plays a key role in the global economy. According to UNCTAD (United Nations Conference on Trade and Development,), during 2018, 80% of global trade was by volume seaborne, which corresponded to be 70% by value (UNCTAD, 2018).

One part of the maritime transport is *Ro-Ro* transport, standing for Roll-on-Roll-off transport, which is indicating that vehicles drive on and off for example a ferry. This is an important form of transport, particularly in United Kingdom, UK (Osborn, 2010). According to (DfT, 2020), during 2019 over 50% of cargo arrivals in the major ports of UK was constituted by $Ro-Ro$ transport.

The Ro-Ro transport brings in turn the topic of linkspan to agenda. Linkspan is a term that is being used broadly in the marine industry, referring to the connection between a vessel deck and a shore on which vehicle can pass at roll-on-roll-off terminals (Osborn, 2010).
A linkspan is of four major types according to (BSI, 2007), these are:

1 the mechanically lifted type, which are by definition hoisted using mechanical lifting equipment, like for instance hydraulic cylinders.

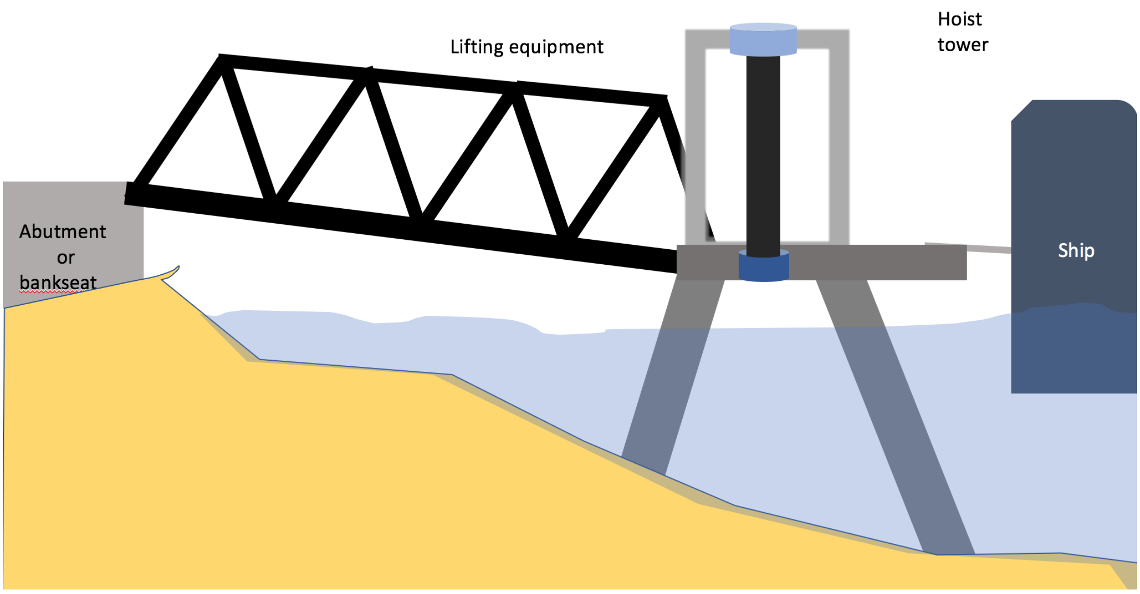

Figure 1.1: A mechanically lifted type

2 the pontoon type, consists of a floating part that is being accessed through a bridge. This means that this can adapt to the incoming tide. The floating part forms the interface with the vessel.

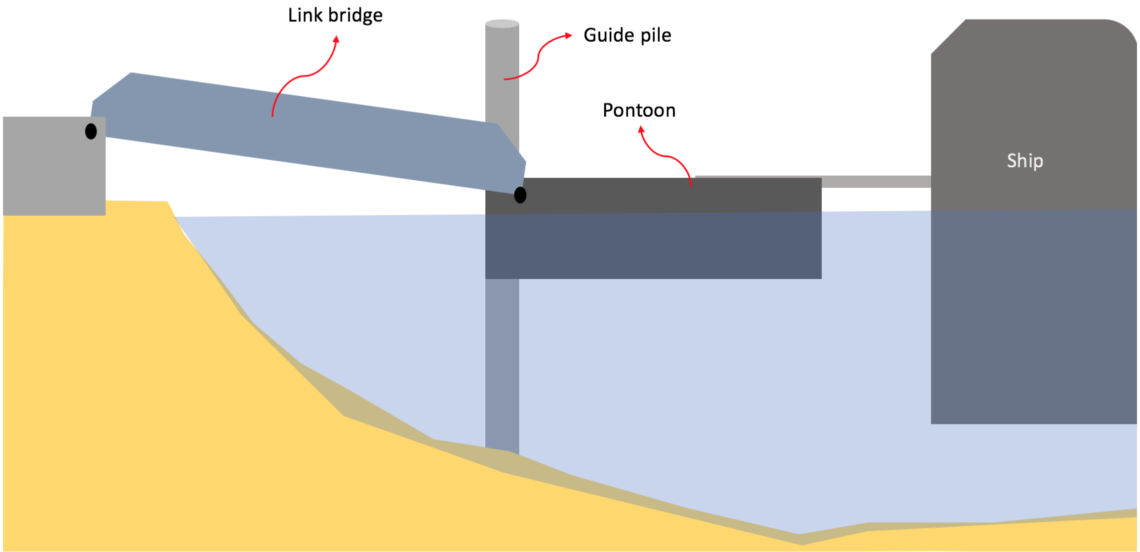

Figure 1.2: The pontoon type

3 the semi-submersible type, is supported by a submerged floating object and a rope is used to give further support by the vessel.

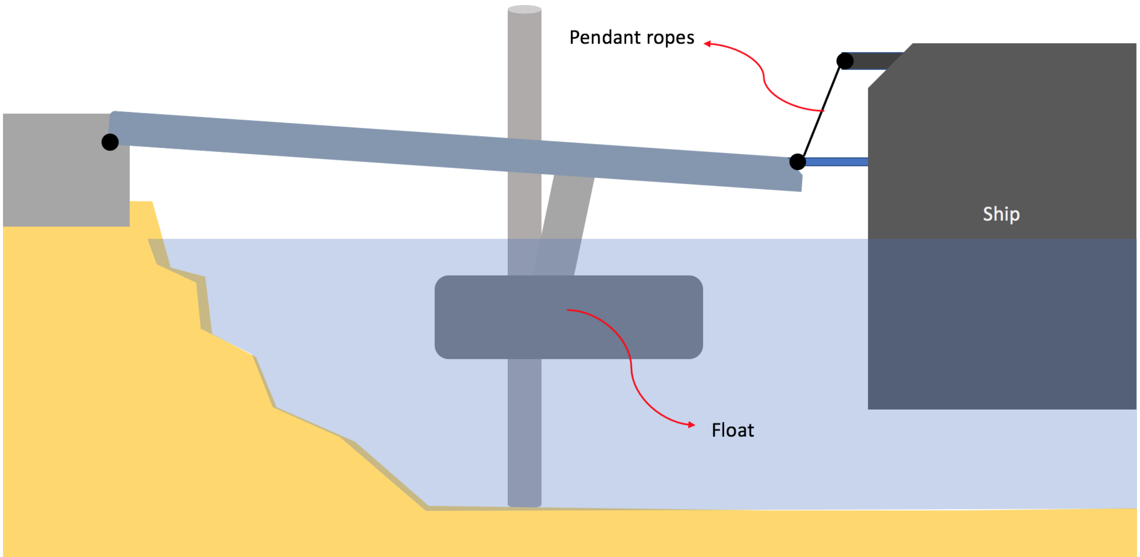

Figure 1.3: The semi-submersible type

4 the integral tank type, which is similar to the second category, but instead with a rigid connection to the bridge.

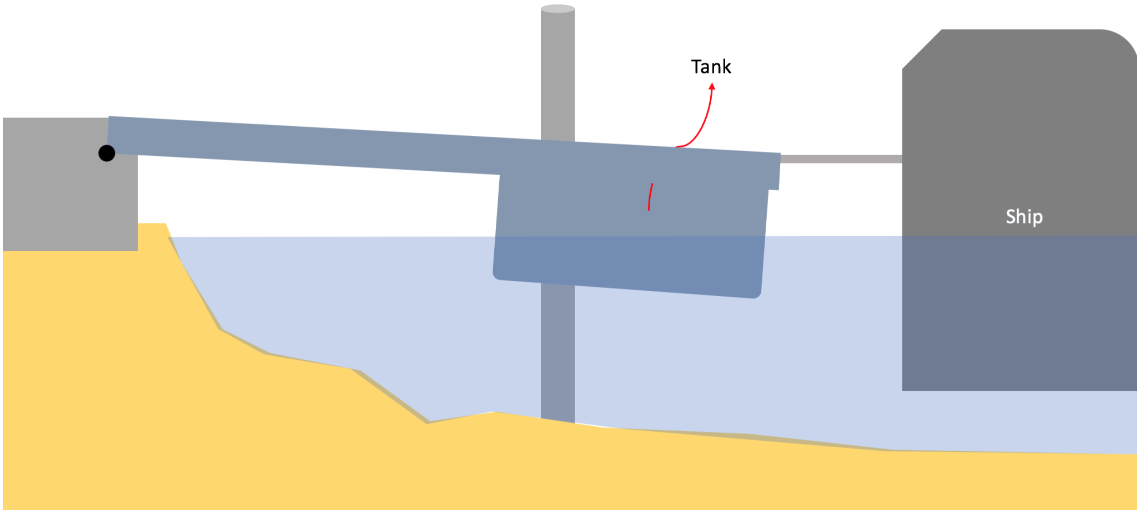

Figure 1.4: The integral tank type

Mentioning the design of these structures, a number of codes of practice are established. *Eurocode* is the most important one (Malm Gustafsson, 2021). It is used to verify the structural strength. Eurocode also includes fabrication and installation procedures. However, Eurocode is limited to only land based structures.

British Standard (*BS*) is often used together with Eurocode, which defines load cases specifically for linkspan and also loads from wave and current (Malm Gustafsson, 2021). Furthermore, *Lloyds's Register* is used. LR is mainly used when the linkspan is to be classified by a third party. The rules of LR covers all aspects of linkspan design and can also be used as reference, even if the linkspan is not to be classed in a classification society (Malm Gustafsson, 2021).

Since these structures are partly floating, wave impact is one of the challenges that engineers have to deal with. According to (Osborn, 2010) there has been a misconception that linkspans are located at a sheltered locations. This is far from the truth, contradictory to this notion, a large number of linkspans are in fact located at places where wave impact is high (Osborn, 2010). The River Mersey in Liverpool is an example. Significant wave heights are in order of 1.5-2 m (Osborn, 2010), which emphasizes the importance of hydrodynamic response awareness of these structures.

Traditionally, tests are conducted in an ocean basin to obtain a prediction of the motion of a floating body. Several numerical methods have been developed to analyse the hydrodynamic behaviour of floating bodies (Ibinabo & Tamunodukobipi, 2019). This is a growing area and there is an increased demand for such simulations, that is because, they are cheaper and easier to perform.

A commercial software for characterizing the hydrodynamic behaviour of floating structures is Ansys Aqwa. It is of interest to analyse global strength of these structures. Thereby, it is beneficial to use hydrodynamic simulation results in combination with structural numerical methods such as Finite Element Method (FEM) to analyze the structure from a strength point of view.

1.1 Aim and Issue

The objective of this thesis consists of two major parts. Firstly, a hydrodynamic study is performed on a floating Integral tank linkspan. The aim is to understand how environmental effects such as waves at different extreme tide levels in addition to extreme loading conditions influence the behaviour of the linkspan in terms of structure motions.

Secondly, the aim is to assess the feasibility of a hydrodynamic load mapping approach for further structural strength FE analyses. These two aims will be accomplished using a 3D radiation/diffraction software called Ansys Aqwa and the FEA program Ansys Mechanical. The project is carried out in collaboration with MacGregor.

1.2 Limitations

The following limitations fall outside the scope of this project:

1. The studied load cases are based only on extreme high and low tidal levels. Reason for this limitation is that meteocean data were provided only for these cases.
2. This study does not focus on structural safety analysis. It means that structural analysis, such as fatigue or ultimate strength is out of scope.
3. Current effects are neglected which in reality exists and can have a significant effect on the simulation results, if accounted for.
4. In this thesis the integral tank concept is used as a case study.
5. In the response analysis, only wind generated waves are taken into consideration.
7. Computation Fluid Dynamics, CFD, simulations are out of scope of this thesis.

2

Theory and Background

This section provides, a theoretical description of hydrodynamic simulations, which are used in this project. This chapter has its main source from Aqwa Theory Manual (ANSYS Inc., 2021a) and lecture notes by (Carl-Erik Janson, 2015). Fig. 2.1 gives an overview of where the different wave theories are applicable.

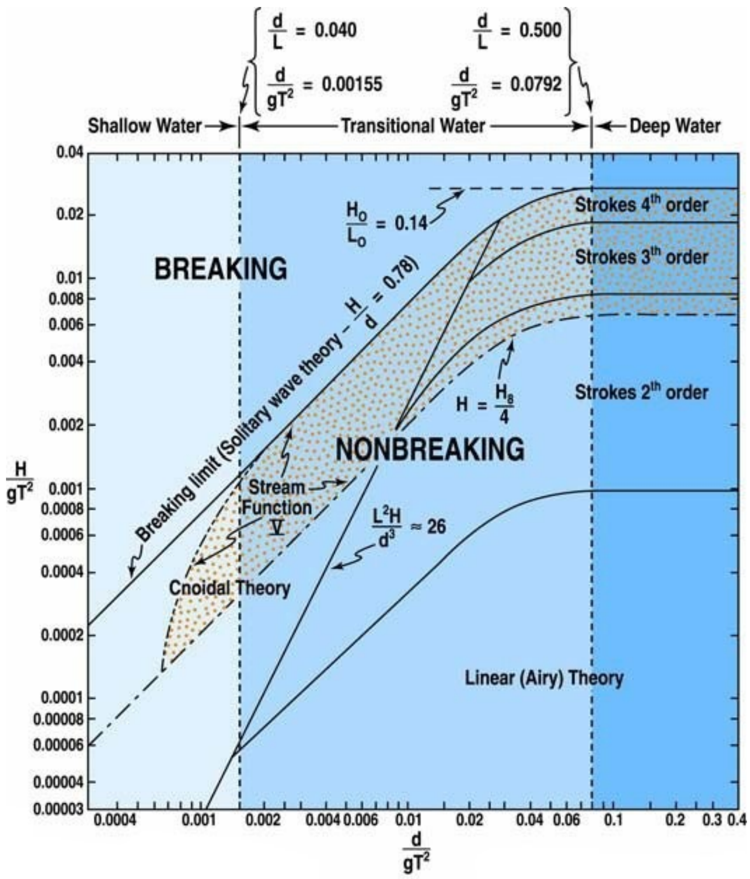

Figure 2.1: Validity regions for different wave theories, according to (Le Méhauté, 2013)

Source Distribution Method approach is employed in Aqwa to solve the Laplace equation, which describes the flow. Hydrodynamic diffraction simulations performed by Aqwa are carried out using Linear Airy wave theory (ANSYS Inc., 2021a) which can be seen in Fig. 2.1 among other theories.

In Aqwa the coordinate system is placed on the still water surface. An example of it can be seen in Fig. 2.2, where the model of the pontoon part, is used in the hydrodynamic study. Since Aqwa is a rigid body analysis program, it is by Fig. 2.2 further illustrated what the different orientations of all degrees of freedom for a rigid floating body are and along which axes they act. The three translations are; surge, sway and heave which are along x, y and z axes respectively.

The three proceeding rotations are denoted roll, pitch and yaw, which are rotate around x, y and z axes respectively.

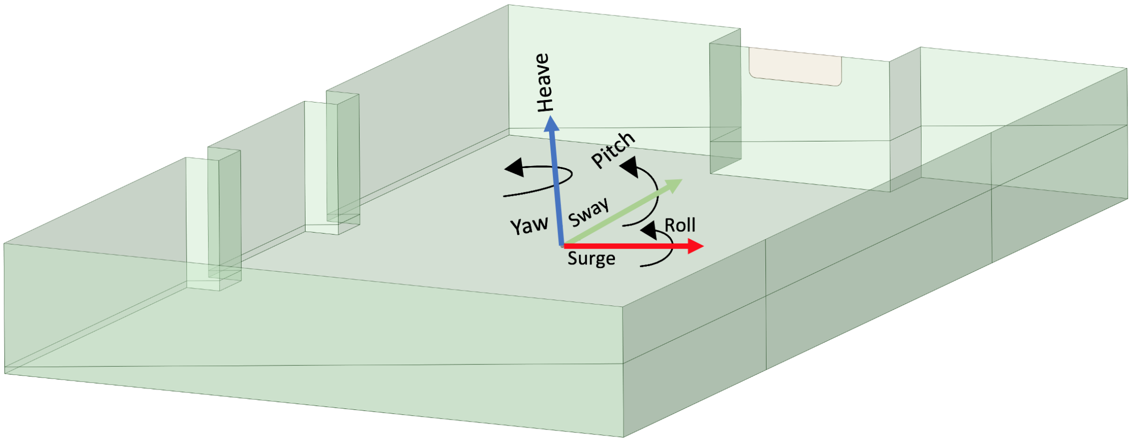

Figure 2.2: Local body motion modes for the pontoon. Red colour implies global x axis, green is y axis and blue is z.

2.1 Basic assumption

In the hydrodynamic field, the flow is normally assumed to be ideal (potential), namely:

- Incompressible
- Inviscid
- Irrotational

Potential theory is applicable for calculation of hydrodynamic parameters such as incident wave force, diffraction wave force and radiation wave force.

2.1.1 Potential theory

Potential flow can be described by potential theory. In this theory, a velocity potential, which is a scalar function, is defined as:

$$\begin{aligned} u &= \frac{\partial \phi}{\partial x} \\ v &= \frac{\partial \phi}{\partial y} \\ w &= \frac{\partial \phi}{\partial z} \end{aligned} \tag{2.1}$$

Substitution of the velocity potential in Eq. 2.1 into the equation of continuity gives the Laplace equation:

$$\frac{\partial^2 \phi}{\partial x^2} + \frac{\partial^2 \phi}{\partial y^2} + \frac{\partial^2 \phi}{\partial z^2} = 0 \tag{2.2}$$

This is a linear second order partial differential equation which can be used to describe small amplitude water wave motion. Adequate boundary conditions are required to solve this equation. Aqwa handle these boundary conditions by itself. However, for illustration purposes, boundary conditions will be mentioned. The boundary conditions are as follows:

1. Linear free surface condition i.e. at $z = 0$:

$$-\omega^2\phi + g\frac{\partial \phi}{\partial z} = 0 \tag{2.3}$$

For linear wave theory this condition means that fluid particles that float on the surface will remain on the surface.

2. Sea bed condition i.e. at $z = -d$:

$$\frac{\partial \phi}{\partial z} = w = 0 \tag{2.4}$$

3. Body surface condition on the mean wetted surface S_0 are defined differently for different potentials:

   - Radiation potential

$$\frac{\partial \phi}{\partial n} = -i\omega n_j \tag{2.5}$$

   - Diffraction potential

$$\frac{\partial \phi}{\partial n} = -\frac{\partial \phi}{\partial n} \tag{2.6}$$

4. An additional boundary to ensure mathematically that radiation waves do not travel in wrong direction.

For further details about how these conditions are employed, it is referred to the Theory Manual of Aqwa (ANSYS Inc., 2021a).

The wave loading under unit amplitude wave $a_w = 1$ is estimated by the potential theory to obtain the Response Amplitude operators, RAOs, see Section 2.3. By harmonic assumption the velocity potential can be written as:

$$\phi(\boldsymbol{x}, t) = a_w \phi(\boldsymbol{x}) e^{-i\omega t} \tag{2.7}$$

where the spatial variation of the velocity potential is described by $\phi(\boldsymbol{x})$.

As stated previously, the Laplace equation 2.2 is a linear differential equation. Using linear superposition, the solutions can be added together according to Eq. 2.8. The spatial part of the velocity potential has three solutions. These are; radiation potential, due to all six rigid body motions as illustrated by Fig. 2.2 (implied by the summation), and a part related to incident wave potential and diffracted wave potential of the wave (ANSYS Inc., 2021a). Superposition reads as:

$$\phi(\boldsymbol{x}) = \phi_1 + \phi_d + \sum_{i=1}^{n=6} \phi_{ri} x_i \tag{2.8}$$

The expression for first order wave potential $\phi_I(\boldsymbol{x}, t)$ is given for finite depth water by linear regular wave theory. By taking the time derivative of the velocity potential, using linearized Bernoulli's equation, the first order hydrodynamic pressure can be obtained:

$$p^{(1)} = -\rho\frac{\partial(\boldsymbol{x}, t)}{\partial t} = i\omega\phi(\boldsymbol{x})e^{-i\omega t} \tag{2.9}$$

For solving the Laplace equation for the three potentials, the source distribution method is employed. This is accomplished by introducing a so called pulsating Green's function that fulfills all condition above.

2.2 Response

As was stated in Eq. 2.7, the velocity potential is following harmonic assumption. This implies that the exciting wave loads, as linear dynamic loads, are harmonically oscillating at a frequency that the structure motion does. This implies that the pontoon is influenced by steady-state wave. The hydrodynamic wave problem is principally classified into two kinds of forces:

1 Wave excitation loads, where Froud-Krylov force is the incident wave force and diffraction force that are induced by disturbance of the incident waves by the non-oscillating body. These forces are thereby independent of the structure oscillation.
2 Added Mass, Damping and restoring forces act on the body when it oscillates at the same frequency as the wave excitation frequency.

2.3 Response Amplitude Operator (RAO)

The harmonic response of a floating body to regular waves are obtained by solving a number of linear algebraic equations of motion. These responses are referred to as *RAOs* and have the unit m/m and $^\circ/m$ which means translational and rotational response per unit amplitude, respectively. The equation of motion reads:

$$\left[-\omega^2\left(\boldsymbol{M}+\boldsymbol{A}\right)-i\omega\boldsymbol{B}+\boldsymbol{C}+\Delta\boldsymbol{C}\right]\left[\boldsymbol{\eta}\right]=\left[\boldsymbol{F}\right] \tag{2.10}$$

Where

$$\begin{cases} \boldsymbol{M} & \text{Structural mass matrix} \\ \boldsymbol{A} & \text{Hydrodynamic added mass matrix for} \\ & \text{all diffracting panel elements calculated by Aqwa} \\ \boldsymbol{B} & \text{Hydrodynamic damping matrix for} \\ & \text{all diffracting panel elements calculated by Aqwa} \\ \boldsymbol{C} & \text{Assembled hydrostatic stiffness matrix calculated by Aqwa} \\ \Delta\boldsymbol{C} & \text{Additional hydrostatic stiffness matrix} \\ & \text{explained in sections 4.2.1} \end{cases}$$

Eq. 2.10 can also be written as

$$\left[\boldsymbol{\eta}\right]=\boldsymbol{H}\left[\boldsymbol{F}\right] \tag{2.11}$$

Where $\boldsymbol{H}=\left[-\omega^2\left(\boldsymbol{M}+\boldsymbol{A}\right)-i\omega\boldsymbol{B}+\boldsymbol{C}+\Delta\boldsymbol{C}\right]^{-1}$ is referred to as the transfer function, relating force to response. It is worth mentioning that the hydrodynamic added mass matrix and damping matrix are all frequency dependent. This equation is solved in frequency domain for a unit wave amplitude to give the structural response, $\boldsymbol{\eta}$.

2.4 Wave induced forces

Wave forces consist of two types, active and reactive (ANSYS Inc., 2021a). The active forces that also are referred to as wave excitation forces, are two types; Froude-Krylov and the diffraction forces (ANSYS Inc., 2021a). The reactive force are created by the structure, inducing wave motions, which also are referred to as radiation forces. For fixed structures the active forces are primarily of significance. On the other hand, for free floating structures, both forces need consideration (ANSYS Inc., 2021a). The wave excitation forces constitute the right-hand side of equation of motion 2.10, and the radiation forces due to damping and added mass take place on the left hand side. Wave excitation forces are in Aqwa calculated as (ANSYS Inc., 2021a):

$$\begin{aligned} F_{Ij} &= -i\omega\rho \int_{S_0} \phi_I(\boldsymbol{x}) n_j dS \quad && \text{incident wave} \\ F_{dj} &= -i\omega\rho \int_{S_0} \phi_d(\boldsymbol{x}) n_j dS \quad && \text{diffraction wave} \\ F_{rjk} &= -i\omega\rho \int_{S_0} \phi_{rk}(\boldsymbol{x}) n_j dS \quad && \text{radiation wave} \end{aligned} \tag{2.12}$$

where in the radiation force matrix for example F_{r33} means heave radiation force due to heave motion of the body. Unit normal n_j corresponds to each rigid body mode $j = 1, 2, 3, 4, 5, 6$:

$$n_j = \begin{cases} n_j & \text{with } j = 1,2,3 \\ \boldsymbol{r} \times n_j & \text{with } j = 1,2,3 \end{cases} \tag{2.13}$$

with $\boldsymbol{r}$ being the position vector for each panel relative to center of gravity. As implied by expressions Eq. 2.12 all of the forces depend on the mean wetted surface. It will determine the number of diffracting panels, in addition to mesh size.

2.5 Wave conditions

A sea state at a stationary form is normally described by two parameters (Det Norske Veritas, 2010); T_p which is referred to as peak period measured in seconds, and significant wave height denoted as H_s measured in meters.

The significant wave height H_s is defined as the mean of one third of the highest (1/3) of a set of wave heights in a certain wave spectrum. The peak period T_p is given by peak frequency ω_p at which the spectral ordinate attains its maximum, as:

$$T_p = \frac{2\pi}{\omega_p} \tag{2.14}$$

where ω_p is expressed in rad/s. According to (Det Norske Veritas, 2010), the Joint North Sea Wave Project, JONSWAP, spectrum is frequently used. It can define a more realistic spectra, because it offers more flexibility with its five parameters. They are chosen from wave statistic combined with systematic parameter fitting (Carl-Erik Janson, 2015). According to Aqwa's theory manual (ANSYS Inc., 2021a), JONSWAP wave spectrum is given by Eq. 2.15:

$$S_{JONSWAP}(\omega) = \frac{\alpha g^2}{\omega^5} e^{-1.25\left(\frac{\omega_p}{\omega}\right)^4} \gamma^{e^{-\frac{(\omega-\omega_p)^2}{2\sigma^2\omega_p^2}}} \tag{2.15}$$

Where

$$\begin{cases} \gamma & \text{peak enhancement factor} \\ \omega & \text{wave frequency in rad/s} \\ \omega_p & \text{peak frequency of the spectrum} \\ \sigma & \text{spectral width parameter} \\ \alpha & \text{factor which relates wind speed to wave frequency} \end{cases}$$

The α factor is computed as:

$$\alpha = \frac{\left(\frac{H_s}{4}\right)^2}{\int_0^\infty \frac{g^2 \gamma^{e^{-\frac{(\omega-\omega_p)^2}{2\sigma^2\omega_p^2}}}}{\omega^5} e^{-1.25\left(\frac{\omega_p}{\omega}\right)} d\omega} \tag{2.16}$$

This means that H_s, ω_p and γ serve as inputs in Aqwa to obtain a JONSWAP spectrum. The spectral width parameter is defined as:

$$\sigma = \begin{cases} 0.07 & \text{for } \omega \leq \omega_p \\ 0.09 & \text{for } \omega > \omega_p \end{cases} \tag{2.17}$$

By defining peak frequency, and the γ (see Eq. 2.15), Aqwa calculates the first and last frequencies based on the following relations, the first frequency calculates as follows:

$$\omega_1 = \omega_p \left(0.58 + \frac{0.05(\gamma - 1)}{19}\right) \tag{2.18}$$

and the last frequency as:

$$\omega_n = \omega_p \cdot F(\gamma) \tag{2.19}$$

where $F(\gamma)$ is a weighting function and for $\gamma = 5$ (see Section 4.2.3) $F(\gamma)$ is equal to $F(\gamma) = 3.70$ and ω is expressed in rad/s (ANSYS Inc., 2021a). According to (Det Norske Veritas, 2010), JONSWAP is reasonable for:

$$3.6 < \frac{T_p}{\sqrt{H_s}} < 5 \tag{2.20}$$

Outside this interval, which is the case for conditions given in Table 4.2, this model is recommended to be utilized with caution. In Aqwa, the required input parameters for the JONSWAP spectrum are T_p and H_s. Given a formulated wave spectrum as above, the wave amplitude for each wave component can be obtained using the following relation:

$$a_i = \sqrt{2S(\omega_i)\Delta\omega_i} \tag{2.21}$$

where $\Delta\omega_i = \omega_{i+1} - \omega_i$, which can in turn be used to calculate each wave height H_i as:

$$H_i = 2a_i \tag{2.22}$$

This will serve as one input to the load mapping, as mentioned earlier in Section 3.1.3.1. This is an irregular wave for which wave surface elevation is computed a summation over n individual regular wave surface elevations:

$$\zeta = \sum_{i}^{n} a_i \cos\left(k_i x - \omega_i t + \varphi_i\right) \tag{2.23}$$

Here, $k_i = 2\pi/\lambda_i$ denotes the wave number for each individual wave. φ_i is a random angle in the range of $0° - 360°$ degrees. n denotes the number of regular waves that are added according to Eq. 2.23, that is 50 using standard settings by Aqwa. Reason for this is to save computational time.

2.5.1 Steepness criterion

According to (Det Norske Veritas, 2010), the following steepness criterion are used in short-term wave response:

$$\begin{aligned} S_S &= \frac{2\pi}{g}\frac{H_s}{T_z^2} \quad \text{with a limit of } S_S = 1/10 \text{ for } T_z \leq 6s \\ S_p &= \frac{2\pi}{g}\frac{H_s}{T_p^2} \quad \text{with a limit of } S_p = 1/15 \text{ for } T_z \leq 8s \end{aligned} \tag{2.24}$$

where T_z, zero-up crossing period, can be for the range of $(1 \leq \gamma \geq 7)$ obtained as:

$$\frac{T_z}{T_p} = 0.6673 + 0.05037\gamma - 0.006230\gamma^2 + 0.0003341\gamma^3 \tag{2.25}$$

This gives a value of $T_z = 2.8664s$ and $T_z = 3.3736$ for case one and two respectively, as per Table 4.2. Using standard earth gravity, $g = 9.80665\ m/s^2$, it can be shown that the steepness criterion for given environmental data will be fulfilled.

2.6 Application of Ansys Aqwa for numerical analysis

Several earlier studies have been carried out for hydrodynamic analysis and load mapping analysis. Some of them are mentioned below.

In a study preformed by (Ibinabo & Tamunodukobipi, 2019) on a Floating Production Storage and Offloading (FPSO) unit, a similar workflow is utilized to determine the RAOs. The hull geometry is considered as a panel model similar to the present thesis work. However, the geometry is modelled by a toolbox named DesignModeler, which is a CAD-program in Ansys. SpaceClaim is used in the present work for modelling. The geometry is sliced by the cut water plane to visualize the draught and the wetted surface. The global coordinate system's origin is located at the stern of the ship, whereas in this thesis, it is located precisely at the middle of pontoon on the water surface level. Mass properties are set as point mass and point buoyancy, similar to the present work, but only with point mass given as input. This is the same as the case of (Wallnöfer, 2015) which will be explained later.

In another study performed by (Masoudi & Zeraatgar, 2017), different breakwater sections and models are being compared based on their response to sinusoidal waves. In this study, the software Ansys Aqwa is used to solve diffraction problem of four different types of breakwater:

- rectangular
- cylindrical
- triangular
- trapezoidal

The study is done by using the boundary element method by means of the above mentioned software. According to the study, for the validation of the results from Ansys Aqwa comparison is made to the previous researches for the rectangular breakwater. This comparison has shown that, given the same weight, triangular breakwater has lowest reflection coefficient and therefore the lowest efficiency. However, rectangular cross Section breakwater has better transmission coefficient among others (Masoudi & Zeraatgar, 2017).

Similarly, in another study on hydrodynamic analysis performed by (Xu, Neng, & Yang, 2019), the three-dimensional potential flow theory and software Ansys Aqwa is used. In this study, a heave compensation system is to be designed and therefore the motion of a mining vessel during operation is analysed. Further in the study, the time-frequency response characteristics of mining vessel under the coupling of wind, wave and flow is analysed by using the mentioned software. The response amplitude operator at various wave headings for all six degrees of freedom at different currents were obtained. RAOs, although on another structure, are also obtained in the present thesis but only considering wave response. The results obtained in the study by (Xu et al., 2019), shows that the wave angle has an influence on the RAOs in all six degrees of freedom and the maximum response angle of the roll is estimated to be 4°. The time domain analysis results expose that the hull roll motion response is larger than the pitch. Furthermore, the effect of sea current velocity on the surge, sway, and heave motion is different. However, the frequency corresponding to the RAO peak is relatively close (Xu et al., 2019).

2.6.1 Load mapping analysis

A research carried out by (Wallnöfer, 2015) pinpoints two steps of analysis. These are determination of the hydrodynamic results primarily such as RAOs, followed by a more detailed global FE-analysis based on the design waves. However, in the case of a more detailed analysis, buckling and fatigue should also be considered according to classification society rules (Wallnöfer, 2015).

The problem of a seamless interface between hydrodynamics and structural analyses were studied in a paper by (Ji et al., 2014). In this study, pressure distribution on hydro model is calculated from sea-keeping analysis and is to be transferred to structural model for estimating structural strength and its integrity. Due to differences in the computation and illustration methods for both analyses, the load on the hydro model may not be fully and correctly transferred to the structural model. This leads to a different load distribution on the structural model, which also in turn is resulting in some unbalanced force and moment components and in this paper a method is introduced to eliminate this problem. This is preformed by applying a pressure distribution on the hydro model, which in turn is mapped on the structural model through projection (Ji et al., 2014). Force and moment imbalances on the structural model are solved by optimization of the nodal forces on the structural model.

Sea-keeping declares motions of a floating body when waves, winds and currents exist. The motions in such conditions can be evaluated using fluid forces that act on a body by means of potential theory. By using the wave load's forces as an input, equation of motion with respect to time is solve for the body. In addition, these calculated loads are important from the structural design point of view, because the body should be designed to keep away from any structural failure under such external loads(Ji et al., 2014).

3 Methodology

The flowchart in Fig. 3.1 visualizes an overview of the workflow in the present thesis. The colours represent certain software programs. The green colour is representing a CAD software, called SpaceClaim that is used for managing the geometries, explained in Section 3.1.1.

Ansys Mechanical is used for the purple blocks, explained in Section 3.1.4. Aqwa package is used for the blue blocks, explained in Section 3.1.2. The workflow can be divided in two major parts. First part is the hydrodynamic part and second part is referred to the load mapping part.

For the *hydrodynamic diffraction*, it is necessary to have a very simplified geometry. Therefore, the provided structural geometry needs to be simplified to obtain a panel geometry model. This is because the Aqwa solver has a limitation regarding diffracting elements, the number of elements should not exceed 30000 diffracting elements. From the hydrodynamic part, RAOs results will be obtained.

In the second part, the provided structural geometry is used to create a mechanical model. In the *equilibrium*, a fixed displacement boundary condition is applied on pontoon bottom (see Fig. 4.1) in order to capture the buoyancy effects in terms of reaction forces and reaction moments. Thereby, a condition for equilibrium to the hydrostatic forces is obtained.

In the next step, *balancing*, the fixed displacement will be removed and the obtained reaction forces and moments are applied instead. Here, the model is sensitive to rigid body singularities if more loading is applied. The model is now ready for load mapping, but the actual load mapping, for which information comes from *AqwaWave* software, is not done yet.

The load mapping is initialized by creating a simplified version of the *Mechanical model.* This is referred to as *ASAS model.* This contains element data for load mapping in terms of ASAS files, which contains the structural information from the ASAS model. Now based on the `.asas` file, AqwaWave generates load mapping files that come from hydrodynamic analysis. Aqwa wave output files contain pressure on each element as surface loads and balancing accelerations, as explained in Section 3.1.3.3.

These are required steps for Aqwa load mapping. Once the load mapping is done, before applying the mapped loads, **weak springs** solver control by Ansys Mechanical is used to prevent rigid body singularities. Results can be reviewed, and load mapping is completed.

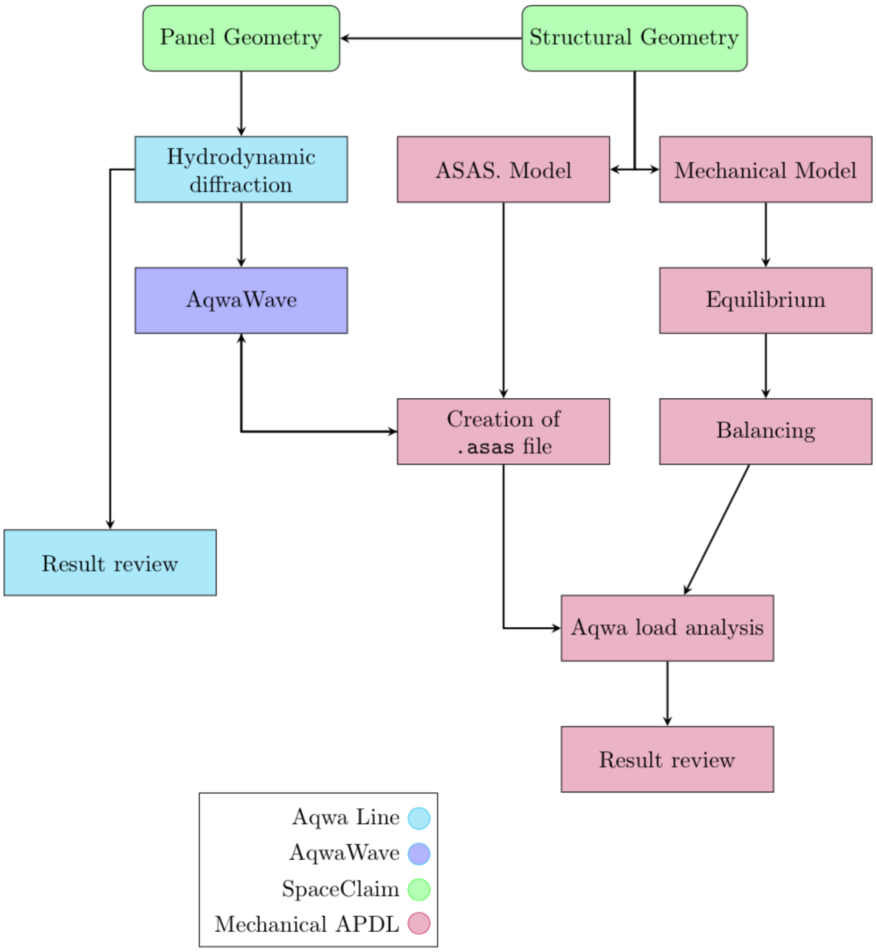

Figure 3.1: Workflow of load mapping with the weak springs solver control

An alternative approach, as illustrated by Fig. 3.2 to the load mapping part will be also investigated. It is called **inertial relief**. This approach calculates balancing acceleration based on the structural model's inertia. Workflow for this approach is a little different. In this approach, the equilibrium and balancing analyses are skipped. Heading directly from the mechanical model to Aqwa load analysis, the inertial relief control solver handles rigid body motions by itself. This approach is expected to give more realistic results. Inertial relief is mainly used in the aviation sector. It should therefore be looked up if the classification rules for marine industry recommends this approach as well.

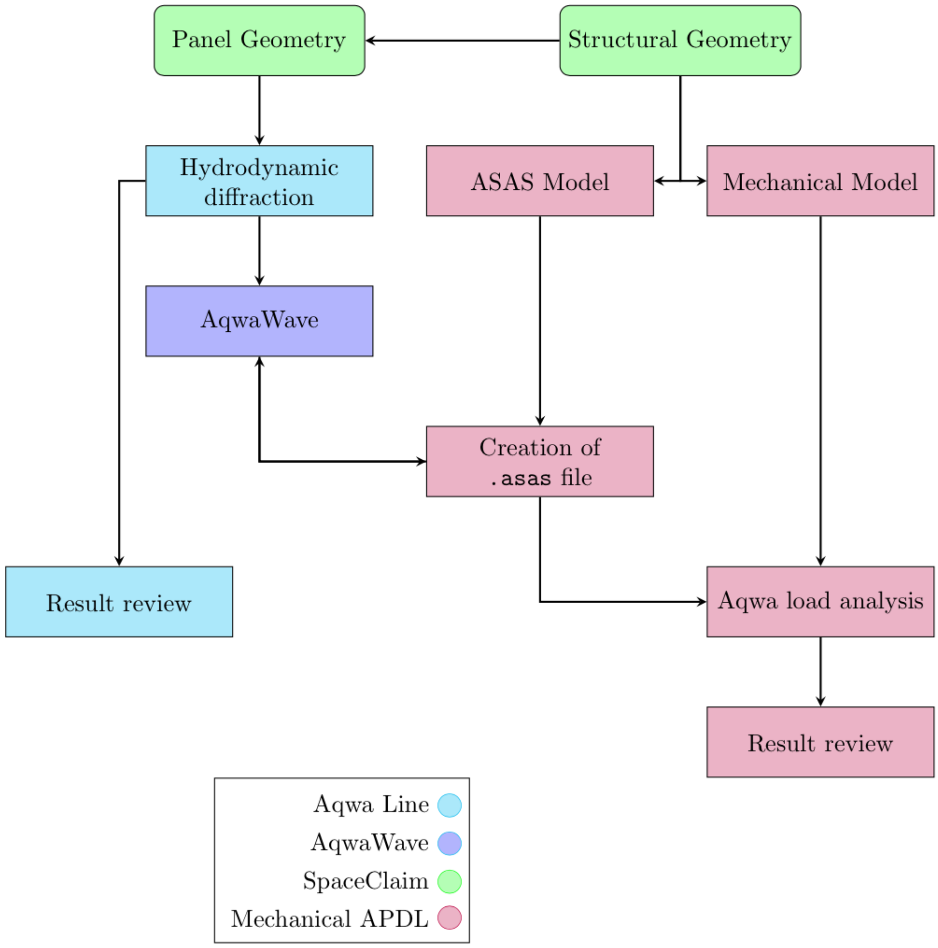

Figure 3.2: Workflow of load mapping with the inertial relief solver control

3.1 Analysis software programs

In this section, the used analysis software are introduced.

3.1.1 SpaceClaim

SpaceClaim is a *modelling* CAD (computer-aided design) program, which is developed by SpaceClaim Corporation. The design capabilities of SpaceClaim are divided into five steps:

- pulling
- moving
- filling
- combining
- reusing 3D shapes

In this project, pulling and moving have been mostly of use.

3.1.2 Ansys Aqwa

Ansys Aqwa is a toolbox within the Ansys package. It provides understanding of the hydrodynamics floating behaviour of marine structures. Ansys Aqwa is accessed through the Hydrodynamic Diffraction and Hydrodynamic Response analysis systems in Ansys Workbench.

Aqwa Hydrodynamic Diffraction is utilized for primary hydrodynamic studies required for further complex response analyses. Here 3D linear radiation and diffraction analysis is done based on inputs such as

- mass properties
- water depth and structure geometry
- wave direction and wave frequency.

Hydrodynamic Diffraction analysis is carried out in frequency domain, that is, Eq. 2.10 is solved for various frequencies defined by the user. The structure geometry is defined by so called panels. The program uses the source distribution approach. Ansys Aqwa is a package that contains many parts. Two of the used parts are:

1 Aqwa Line is a 3D diffraction and radiation analysis software that is utilized for hydrodynamic and hydrostatic calculations. Theory that is used for this part is explained is the theory chapter.
2 AqwaWave works as a link between Aqwa Line to transfer hydrodynamic loads to the FE program Mechanical APDL for strength FE analysis.

3.1.3 AqwaWave

AqwaWave is the link between the hydrodynamic model and structural model and is a part of the Aqwa package. Load mapping is a process involving the transfer of wave loads on a floating structure explained in Section 3.1.2 to a FE model for further structural analyses such as global stress analysis.

Hydrodynamic diffraction analysis results in a set of pressures that are being calculated at the centroid of the panels. These are a result of incident, diffracted and radiated waves, and additionally hydrostatic variation for a user-defined interval of wave periods and headings. However, this pressure is related to a unit wave amplitude, and when a certain wave height is defined by the AqwaWave user, this pressure is scaled by AqwaWave (ANSYS Inc., 2021b). The pressure consists of a real and an imaginary part.

3.1.3.1 AqwaWave Input

AqwaWave transfers a wave load-case, that is specified by (ANSYS Inc., 2021b):

1. Frequency ID, that is the frequency number in the hydrodynamic diffraction analysis, applied to the floating body (in this case the panel model).
2. The next input, direction ID, which is the heading angle of the wave, is measured relative to the global X axis.
3. The wave height, which is the double of the wave amplitude is the next input.
4. The wave phase angle φ in degrees, is used according to

$$dt = T \cdot \frac{\varphi}{360} \tag{3.1}$$

where dt is the elapsed time since a wave crest progressed through the COG of the structure. Here T is the wave period. φ is positive.

An example of an input data file can be found in Appendix A.1. This is used to generate the load mapping from Ansys Aqwa to Ansys Mechanical.

Running AqwaWave requires three major components (ANSYS Inc., 2021b):
1. An input data file is used as a reference to process the Aqwa hydrodynamic and structural files, including load generation from the available Aqwa model.
2. An `.asas` file, is created by running the APDL command `ANTOASAS` in Static Structural that is an Ansys Workbench analysis system. This step is further explained in Section 3.1.3.2.
3. Database for the Aqwa model that is used, is obtained by running an analysis of hydrodynamic diffraction. This is another Ansys Workbench analysis system.

3.1.3.2 Asas model

The `ANTOASAS` APDL command in Ansys Mechanical generates an `.asas` file from which model information is obtained from the database for FEA system, which is established on a chosen set of elements. The following data is sorted in such file:

- Nodes
- Elements
- Material data
- Geometry data
- Section data
- ANSYS element components (ASAS sets)
- Boundary conditions
- Loads
- Solution control options

The `.asas` model is chosen to be the wetted surface on which the hydrodynamic diffraction analysis by Aqwa is conducted.

3.1.3.3 AqwaWave Output

By running AqwaWave, load information files are generated, and are called according to `file_aqld####.dat` with digits 1001 for the first load case. This file gives pressure distribution information on each FE mesh element, in addition to balancing acceleration (ANSYS Inc., 2021b) which constitutes the inertial loads. Load result files will give the following APDL command:

$$\text{SFE},\ \text{Elem},\ 2,\ \text{PRES},\ 0,\ \text{VAL1},\ \text{VAL2},\ \text{VAL3},\ \text{VAL4}$$

Here, `SFE` is an ADPL command intended to specify surface loads on elements. Its inputs are given thereafter. Elem denotes the element number on the FE model on which the surface load will act.

The value 2 is used to give a specification on points. PRES is a Surface Load Label that denotes pressure. The input value 0 implies further that VAL1 to VAL4 are the real components of the pressure. For further information on SFE comand it is referred to APDL manual.

The interpolation by AqwaWave consists of three steps:

1. Extracting panel pressure from the hydrodynamic solution.
2. Transferring the pressure from centroid to the connected panel nodes through weighted averaging as per Fig. 3.3.

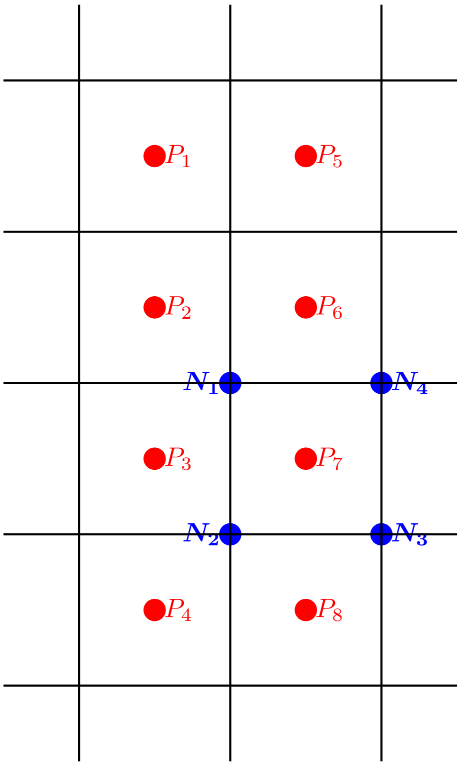

Figure 3.3: Panel pressures that are stored at panel centroid are extracted and interpolated to the Aqwa element (panels) nodes.

3. Locating the FEM model mesh on the Aqwa mesh and interpolate the pressure from panel nodes to FEM element nodes, as portrayed by Fig. 3.4.

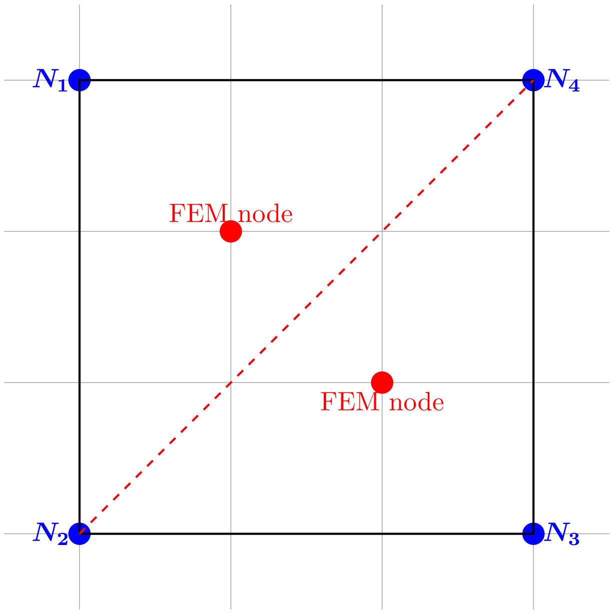

Figure 3.4: An example of interpolation from Aqwa panel to FE element.

3.1.4 Ansys Mechanical APDL

Mechanical APDL is a large-scale and multipurpose finite element program in which different engineering problems can be solved. It can analyze the following problems:

- static structural
- dynamic structural
- steady-state and transient heat transfer problems
- mode-frequency and buckling eigenvalue problems
- static or time-varying magnetic analyses

and various types of field and coupled-field problems (ANSYS Inc., 2013a).

4

Basis of the analysis

In this chapter, input parameters and how the simulations are set up will be explained. It starts with a brief introduction to the studied geometry. Thereafter, hydrodynamic diffraction simulations are explained, and the different load cases are presented. It is explained also how structural behavior in terms of roll and stiffness are captured in the hydrodynamic analysis. Last part of the chapter is about load mapping and how different boundary conditions are defined in the FE model.

4.1 Features of the geometry

Fig. 4.1 visualizes the different parts of the studied geometry. In Section 4.2 the pontoon part is considered. This includes the forward part of the model, where river side, pontoon bottom, ship side and shore side are different parts. However, in the hydrodynamic model, only the outer surface is considered as it was visualized by Fig. 2.2. Structural steel is the material that is used in the model.

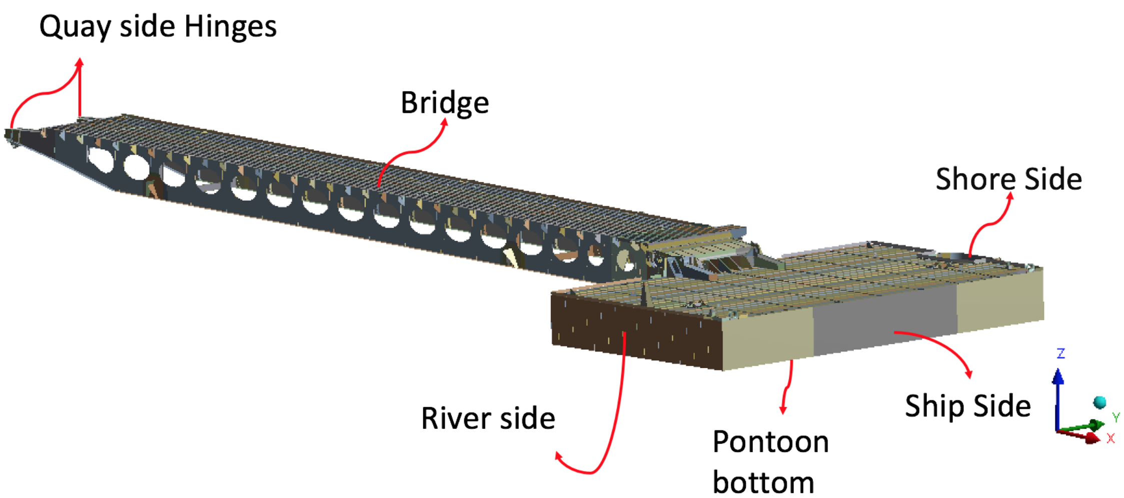

Figure 4.1: Geometry features

4.2 Hydrodynamic diffraction simulations

In this thesis hydrodynamic diffraction simulations are performed at four load cases, presented in Table 4.1.

Table 4.1: Load cases

Load case	Combinations
1	Lowest Astronomical Tide with self-weight condition
2	Lowest Astronomical Tide at fully loaded condition
3	Highest Astronomical Tide at self-weight condition
4	Highest Astronomical Tide at fully loaded condition

Extreme tide levels Lowest Astronomical Tide (LAT) and Highest Astronomical Tide (HAT) give a water depth of $d = 5.11$m and $d = 15.71$m respectively, which makes the structure to pitch at $5.71°$ (clockwise) and $-2.61°$ (counterclockwise) respectively. Mass data for loaded and self-weight conditions is explained in Section 4.2.4.

Common for these conditions is solving Eq. 2.10 at various frequencies. However, these frequencies are in this thesis given in different ways. First part is based on a periodic interval of $1.2 - 30s$. In Aqwa it is possible to define this interval using two further possible ways, illustrated by Fig. 4.2. While load case 2 as per Table 4.1 is simulated period based interval division according to Fig. 4.2b, other three cases are simulated using frequency based interval division, according to Fig. 4.2a. This means that for the frequency based interval division, the "mesh" is much finer at small wave periods. It can be thought of as a geometric progression shaped mesh. For the period based interval division, calculation points are instead uniformly distributed.

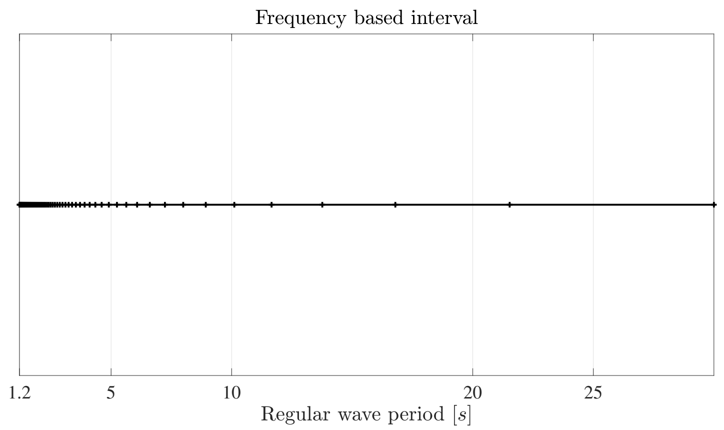

(a) Frequency based interval

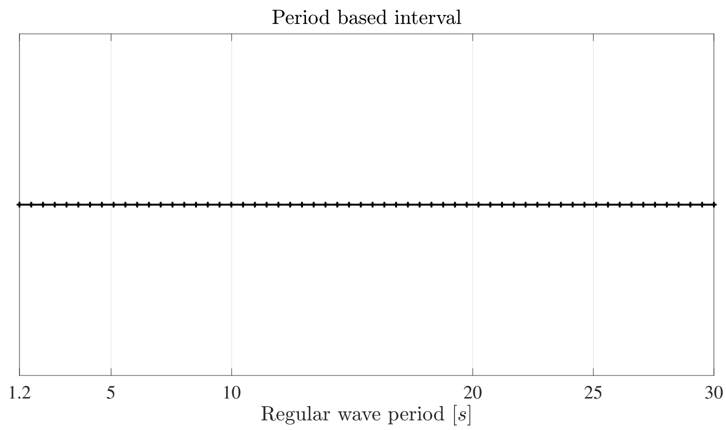

(b) Period based interval

Figure 4.2: Illustration of the two different interval division. Each calculation point is marked by a plus sign.

Wavelengths for this set of period can be seen by Fig. 4.3. These are calculated using a code programmed by (Gabriel Ruiz Martinez, 2021), which calculates dispersion relations for water waves using Newton-Raphson's method. Shallowness of the water waves is based on Fig. 2.1. As implied by Fig. 4.3b no shallow water waves appear at HAT due the higher water depth.

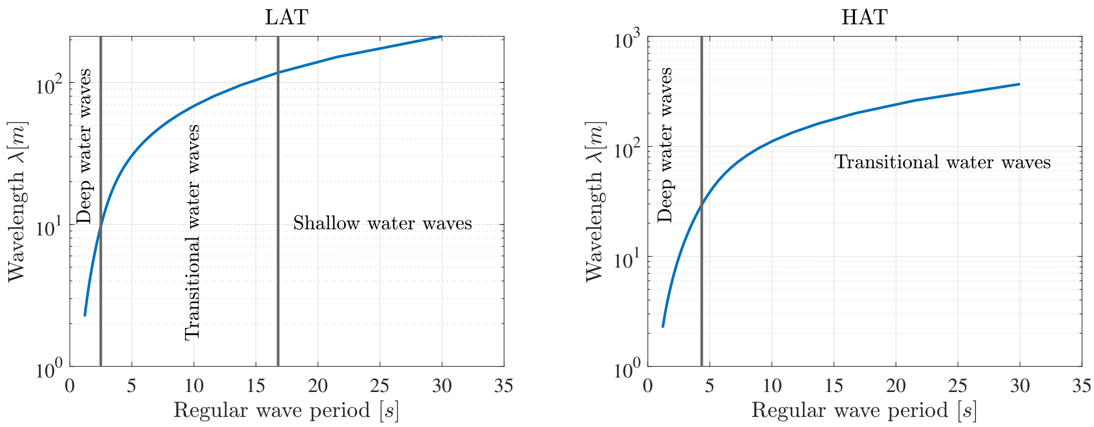

(a) Depth $d = 5.11$m

(b) Depth $d = 15.71$m

Figure 4.3: Wavelengths for the present set of periods.

RAOs are obtained for stated wave periods to visualize the structural response. Furthermore, wave excitation forces as explained in Section 2.4, are obtained and will be discussed in the results section. Thereby, an overview of the wave impact is achieved and the coupling of wave excitation force to RAOs will be discussed. Since the structure is in fact prevented from translating in x and y directions, RAOs for surge, sway and yaw are not considered in the hydrodynamic analysis. However, pitch, roll and heave motions are resonant modes for floating bodies (Carl-Erik Janson, 2015). The pontoon is simulated as a floating body. In the load mapping analysis surge, sway and yaw motions play an important role in terms of interface forces and accelerations.

The second set of the hydrodynamic diffraction simulations are carried out using a formulated wave spectra. Here meteocean data in Section 4.2.3 results into two cases, where the goal is to map the obtained solutions to the FE-model of the linkspan.

4.2.1 Stiffness evaluation

In order to capture the stiffness behaviour in the different orientations, two load cases in terms of roll and pitch have been performed according to Fig. 4.4. Here, prescribed rotations at 1-5 degrees are applied along each axis to give a trend line. The slope of each line shown in Fig. 4.5a and 4.5b, will be used as additional restoring hydrostatic stiffness to Aqwa. Roll and pitch stiffness are given as ΔC_{33} and ΔC_{44} components of the additional hydrostatic matrix, $\Delta \boldsymbol{C}$, in Eq. 2.10 in Aqwa.

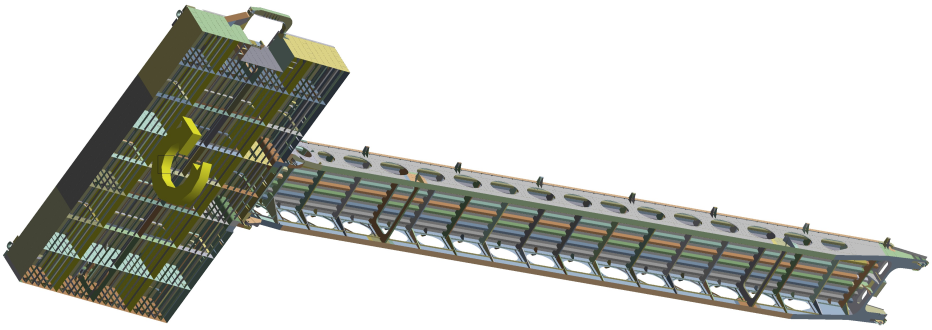

(a) Roll

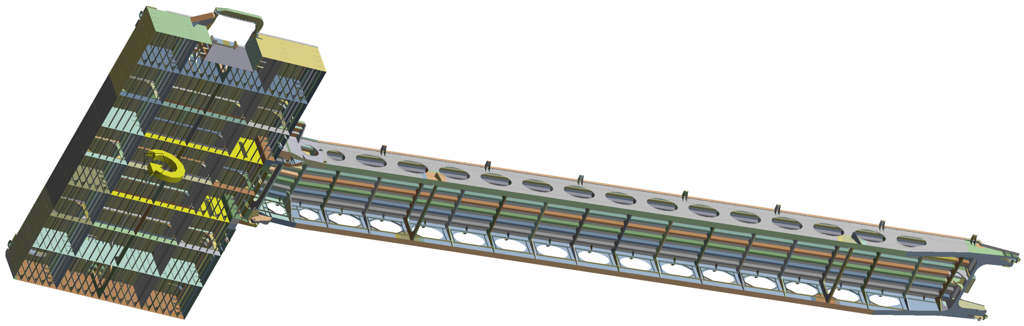

(b) Pitch

Figure 4.4: Prescribed rotations to capture the structural stiffness behaviour.

Fig. 4.5 gives a visualization of the structure stiffness. Roll stiffness is calculated with respect the transverses as portrayed by Fig. 4.4a. Stiffness in pitch is similarly obtained with respect to longitudinal plates.

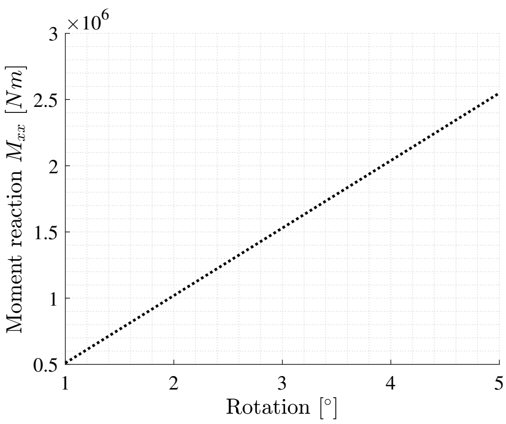

(a) Reaction moment vs rotation around x-axis

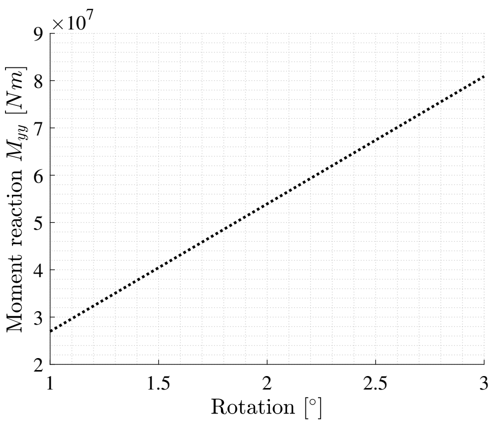

(b) Reaction moment vs rotation around y-axis

Figure 4.5: Stiffness evaluation based on the FE model of the linkspan

A linear expression for Fig. 4.5a is:

$$M_{xx}(\theta_x) = 5097850\theta_x - 24 \tag{4.1}$$

Resulting in a torsional stiffness of 50.9785 $kNm/°$ which will be given as additional hydrostatic stiffness to hydrodynamic analyses.

Fig. 4.5b gives an illustration of the structural stiffness around $y - axis$ with respect to transverse stiffners according to Fig. 4.4b. As it is illustrated, for each degree rotation a significantly higher pitch moment is required. A linear expression for Fig. 4.5b is:

$$M_{yy}(\theta_y) = 26968500\theta_y + 333 \tag{4.2}$$

Resulting in a torsional stiffness of 26968.500 $kNm/°$ which will be given as additional hydrostatic stiffness to hydrodynamic analyses. As mentioned earlier, this is a much higher value than the roll's stiffness.

4.2.2 Wave directions

Fig. 4.6 illustrates the different wave angles that are employed in the analysis. As per Fig. 4.6, two cases; one beam and one head sea are chosen for which the results will be presented. Results for the rest of directions are presented in Appendix. The position of fixed reference axes, where Center of Gravity (COG) lies, is shown as well. However, the position for COG can differ from case to case.

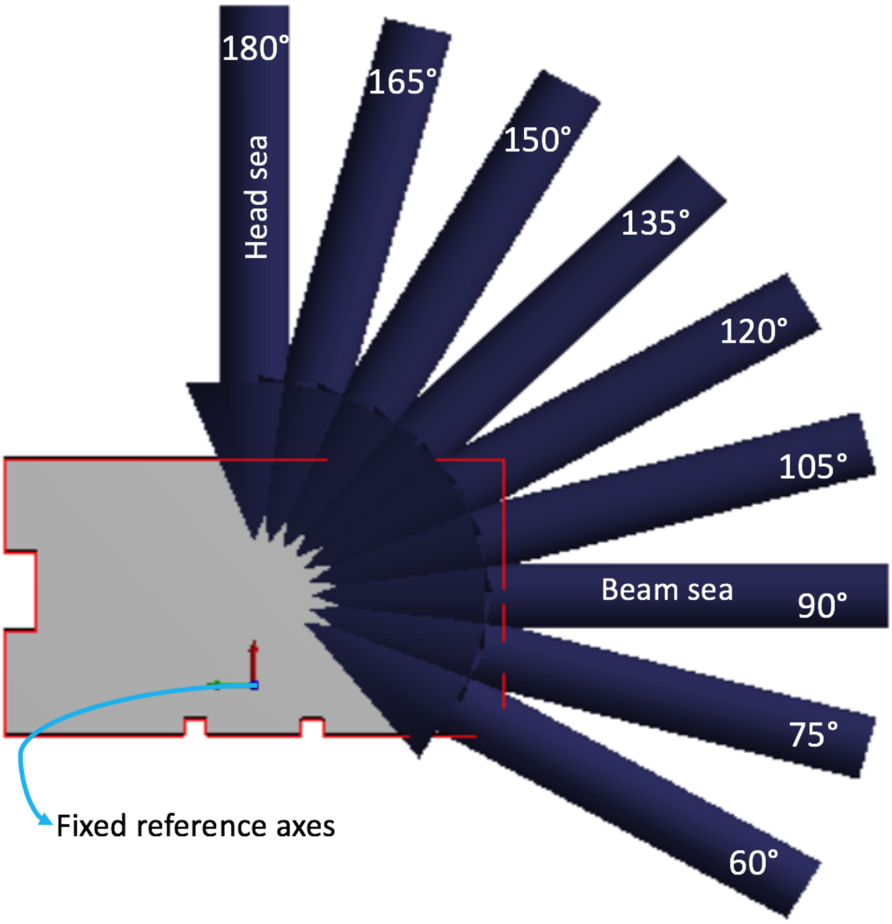

Figure 4.6: All wave directions spanning from $60° - 180°$, where beam and head sea are illustrated.

4.2.3 Design waves

Based on the metocean data report (Chamberlain, 2020) a number of environmental conditions are defined according to Table 4.2. These are defined using two discrete JONSWAP wave spectra, that are plotted in Fig. 4.7a.

Table 4.2: Design Waves

Design wave	Return period	significant wave height H_s [m]	peak period T_p [s]
1	1 year	1.22	3.56
2	100 year	1.76	4.19

According to meteocean data provided by (Chamberlain, 2020), Table 4.2 data are based on locally generated wind within the Mersey river. According to recommendation of (Det Norske Veritas, 2010) for the ratio of $T_p/\sqrt{H_s} \leq 3.6$, the peak enhancement factor for the defined JONSWAP spectra is set to $\gamma = 5$.

Fig. 4.7a illustrates two JONSWAP spectra for the conditions that are mentioned in Table 4.2. Here, the peak period is instead given as peak frequencies according to Eq. 2.14. As implied by Fig. 4.7a, the major part of the wave energy is located between a period range of 2-6 seconds. Fig. 4.7b visulizes the amplitude spectrum. It is calculated using Eq. 2.21. The amplitudes are doubled to give the wave heights that are used as an input to the load mapping.

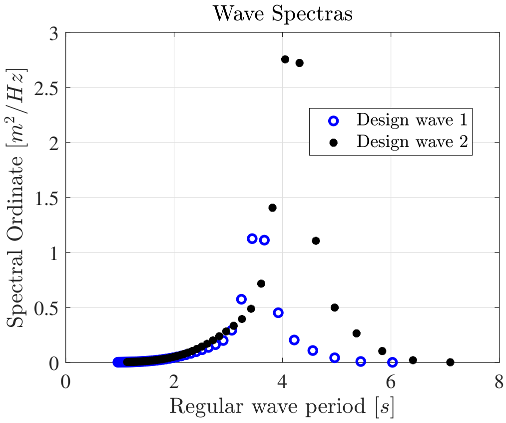

(a) Wave spectrum.

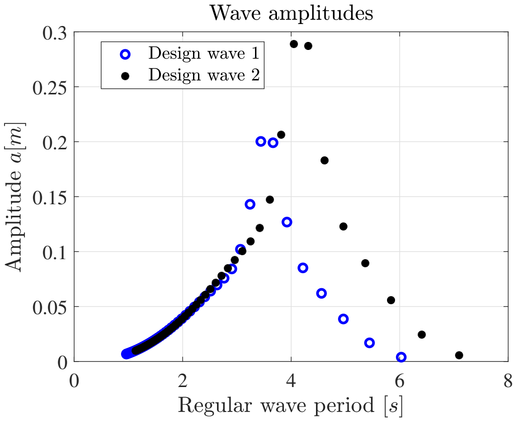

(b) Amplitude spectrum.

Figure 4.7: Wave and amplitude spectrum.

In order to keep the extent of the thesis reasonable, load mapping analyses are performed on the empty loaded hydrodynamic diffraction analyses as per Table 4.3.

Table 4.3: Extent of the load mapping

	Wave heading [°]	Design wave
LAT	90, 180	1
HAT	90, 180	2

4.2.4 Mass and geometrical data

Table 4.4 presents mass input data for the hydrodynamic diffraction analysis. Data from Table 4.4 defines the structural mass matrix in Eq. 2.10. The draught will determine the wetted surface for which diffracting elements will exist. At these diffracting elements the software will solve the hydrodynamic problem using potential theory explained in Section 2.1.1.

Table 4.4: Mass input data for hydrodynamic diffraction analysis

	Empty Loaded	Fully Loaded
Mass on Pontoon $[kg]$	367668	535034
Draught $[m]$	0.92	1.34
x $[m]$	-3.88	-5.15
y $[m]$	0	0
z from pontoon bottom $[m]$	1.70	4.083

The above data are adapted to the draught, and the pitching angle mentioned in Section 4.2.3 . Additionally, radii of gyration are given measures. Radii of gyrations are depending on geometry and mass distribution which is structure itself, load, and ballast water if exists. Following relations relate radii of gyration to moments of inertia around each axis:

$$\begin{aligned} I_{xx} &= m \cdot k_{xx}^2 \\ I_{yy} &= m \cdot k_{yy}^2 \\ I_{zz} &= m \cdot k_{zz}^2 \end{aligned} \tag{4.3}$$

Here m is the total mass, and k_{xx}, k_{yy} and k_{zz} denotes radius of gyration around respective axis. Table 4.5 gives input values of the different radii used in the analysis.

Table 4.5: Radii of gyration

	Empty load	Full load
$k_{xx}[m]$	6.56	6.38
$k_{yy}[m]$	10.65	19.53
$k_{zz}[m]$	12.07	19.85

4.2.5 Panel models

Two examples of calculations models used in Aqwa are illustrated in Fig. 4.8. The green sphere indicates the defined point mass. It is the mass of the structure (including the bridge part as well) as per table 4.4. The different pitch angle and different water depth is visualized in Fig. 4.8. It can be observed that due to different pitching angles (around y axis) mentioned in Section 4.2.3 different water displacements occur. For example, in Fig. 4.8a the displacement is larger due to the larger pitching angle than HAT in Fig. 4.8b, despite the same draught. A mesh with maximum element size of 0.25m is used in the panel models to be able to simulate the minimum period of $T = 1.2$s.

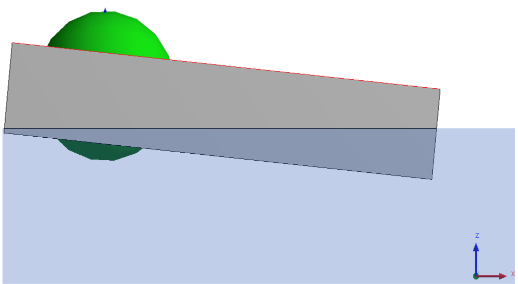

(a)

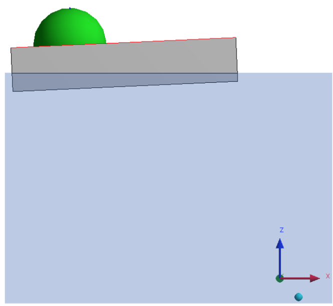

(b)

Figure 4.8: Calculation panel models used in Aqwa for the two self-weight load cases.a)LAT empty panel model with pitch angle (around y axis) 5.71°. b) HAT empty panel model with pitch angle (around y axis) $-2.61°$.

4.3 Design wave load mapping

This part of the thesis is realted to the FE model presented in Fig. 4.1. In this part, a very fine mesh with maximum element size of 0.2 m is used.

4.3.1 Boundary conditions

In order to capture the correct structural behaviour, it is crucial to have proper boundary conditions. The boundary conditions of the hinge structure is visualized by 4.9.

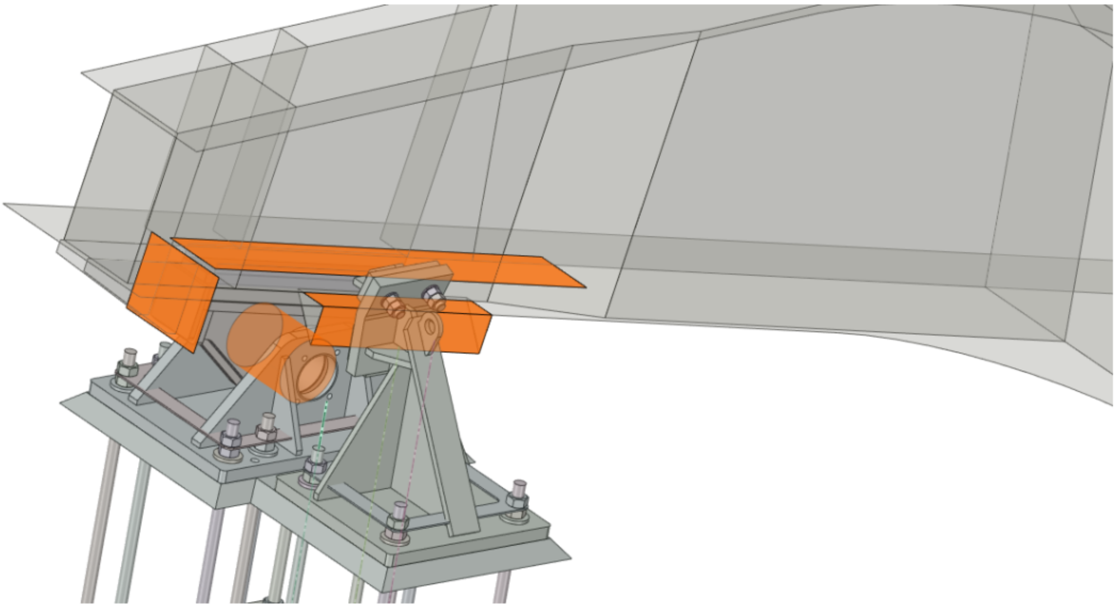

Figure 4.9: Hinge conditions

The hinge structure has the following boundary condition:

1. Free rotation around y axis.
2. Fixed translation in y direction.
3. Fixed translation in z direction.
4. Fixed translation in x direction.

Furthermore, there are additional fixed y translation boundary conditions. according to Fig. 4.10 near the shore side shown in Fig. 4.1, there is a pile gives fixed y translation.

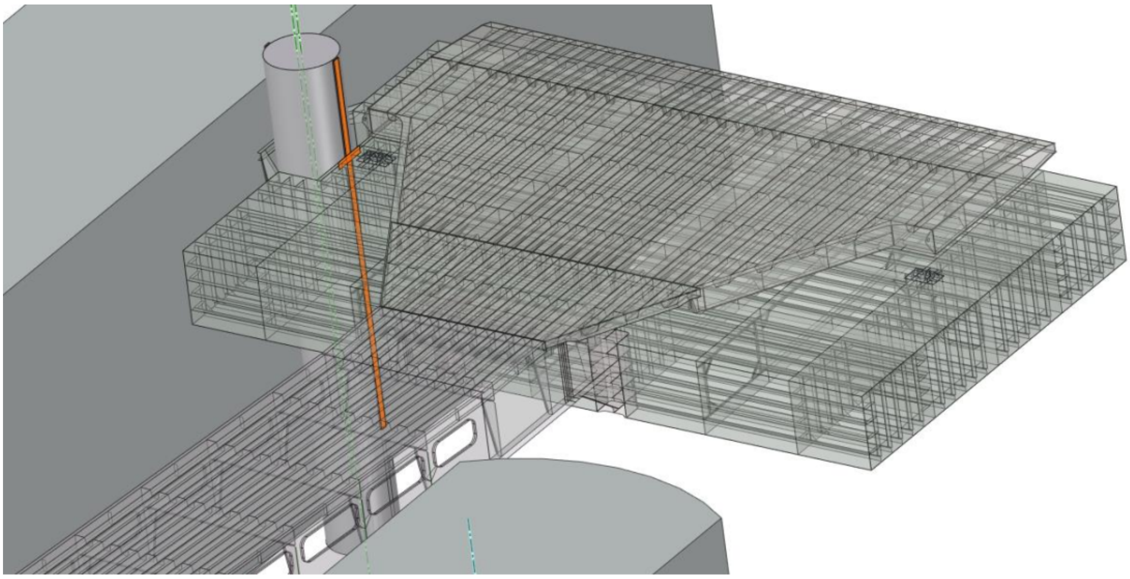

Figure 4.10: Pile conditions

In addition to this, since the structure is at a floating condition, buoyancy force is considered. Here, initially, a fixed displacement boundary condition, i.e. fixed translations and rotations is applied to the pontoon bottom, as visualized by Fig. 4.1, in order to capture the buoyancy effects in terms of reaction force and reaction moment. This is thereby a condition for equilibrium to the hydrostatic forces. However, when the fixed displacement is removed, the reaction forces and moments are applied instead.

At this stage, the structural model is unstable due to rigid body motion. Ansys Mechanical has a solution to tackle this problem, called weak spring conditions. By enabling this option, rigid body motion singularity are removed automatically which results in a reasonable solution to the problem of free floating. For the weak springs option, the balancing accelerations as a result of the mapping pressures are based on the Aqwa model's mass and inertia matrix applied.

A solver control option employed in the analysis for comparison purpose is inertial relief. This option calculates the balancing accelerations based on the FE model. These are based om mass and inertia matrix information that Ansys Mechanical calculates. Inertial relief option, like weak springs option, is able to handle the issues related to rigid body motion as well.

A top view of the boundary conditions can be seen in Fig. 4.11. Hinge boundary conditions are explained earlier. The conditions for pile are seen as well.

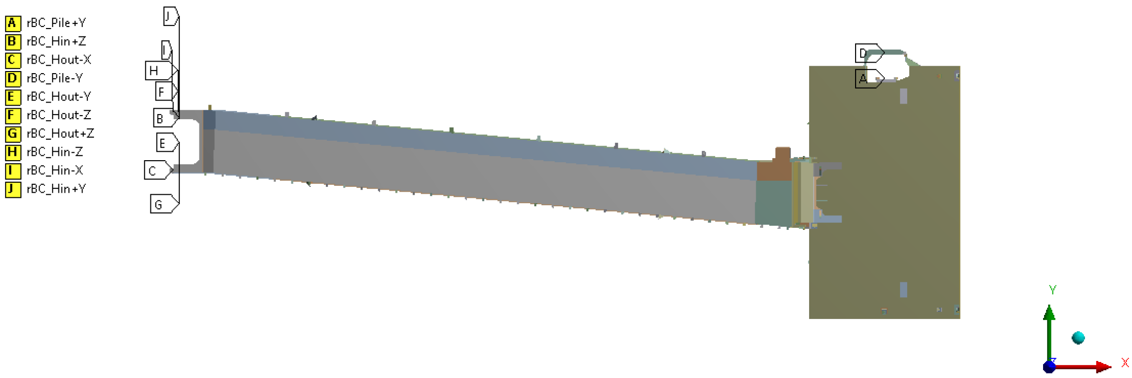

Figure 4.11: Boundary conditions in the linkspan model

5

Results and discussion

In this chapter, simulation results for both the hydrodynamic and the load mapping part are presented.

5.1 Rigid body hydrodynamic diffraction analysis

In the upcoming subsections, in order to facilitate the explanation of the underlying physics, the worst case results in terms of wave direction is taken into consideration. RAOs are implied via equation of motion (Eq. 2.10) and they are related to wave excitation forces and moments. Three types of forces caused by waves are accounted for in this analysis. The first one is radiation waves which are induced by structure motion in waves and are on the left hand side of the Eq. 2.10, including added mass force, radiation damping and hydrostatic restoring stiffness. The other two are incident wave and diffracting wave, which are usually mentioned together. They constitute the wave excitation effect and are external forces that act on the structure. They are defined on the right hand side of Eq. 2.10 and generate the structure response. An example for the HAT full case in 90° is illustrated in Fig. 5.1 and Fig. 5.2, it is calculated by Aqwa using a wave grid. Fig. 5.1 shows that the waves travel perpendicular to the structure. The diffraction waves can be see in the upper part of the Fig. 5.1, where they are disturbed by the stationary structure.

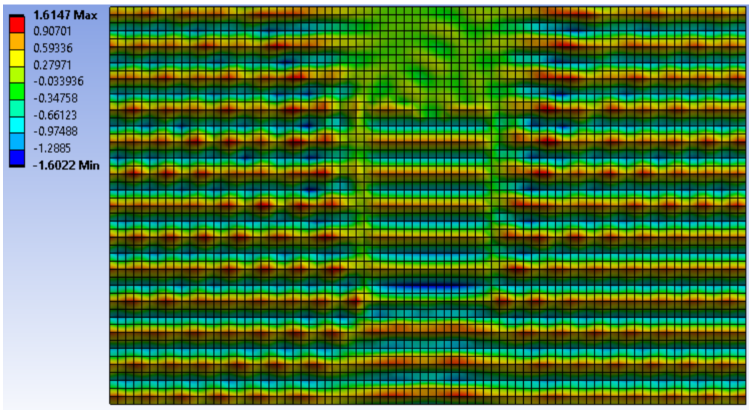

Figure 5.1: Incident and diffracted wave surface elevation in meters at $T = 1.63$ s

It can from Fig. 5.2 be observed that radiation waves travel in radial direction. Incident waves are undisturbed waves, that after collision with the body and becomes disturbed, scattered and constitute the diffracting waves. At smaller wavelengths as in this case, it can be seen that radiation waves are smaller in terms of surface elevation. In the upcoming sections, contour plots for wave surface elevation including the combined effect of these three waves will be shown.

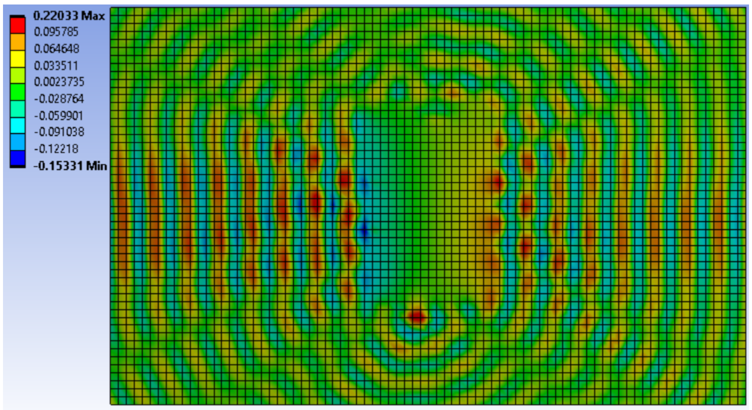

Figure 5.2: Radiation wave surface elevation in meters at $T = 1.63$ s

5.1.1 Heave

Fig. 5.3a shows the heave response in different load cases for 180° waves.

As shown in Fig. 5.3a, the heave response amplitude is in the vicinity of 1 m per unit wave amplitude, which is not significant in our case. This is indicative of the additional restoring stiffness in pitch, as explained in Section 4.2.1, that is able to dampen the heave amplitude.

An observation from Fig. 5.3b is the sudden break in the continuity of the LAT full and empty graphs. The reason for this is that present wavelengths are smaller in the case of LAT. It can also be confirmed by Fig. 4.3a. The reason for smaller wavelengths at LAT is related to the water depth which is smaller than HAT.

Another observation related to LAT graphs in Fig. 5.3 is that there is no well-defined peak response in comparison to HAT graphs. This can be explained by the pitch angle, which is larger in LAT, 5.71°, and pointing downwards. As shown in Fig. 4.8b, the panel model for HAT pitches counterclockwise and thus is less favourable for incident 180° (head sea) waves.

In pitch as mentioned in Section 4.2.1 there was an additional restoring stiffness. Since it was able to dampen the response, it means that there is a heave-pitch coupling. The restoring pitch stiffness "delays" maximum response in terms of wavelengths if it would be compared to roll results in Fig. 5.6b where the additional restoring roll stiffness is smaller.

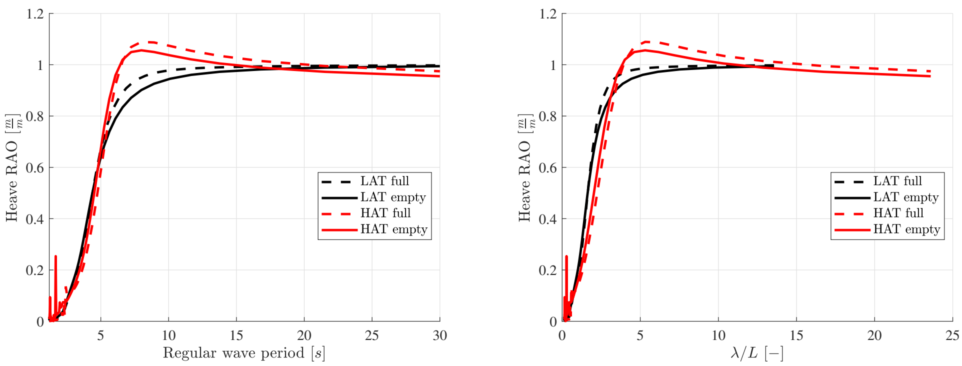

(a) Heave RAOs at different periods

(b) Heave RAOs at different λ/L

Figure 5.3: Visualization of heave response for different load cases at 180° waves. L is the length of the pontoon and λ is wavelength.

Fig. 5.4 illustrates the peak response scenario given in Fig. 5.3a for HAT empty case. This contour plot shows that wavelength is approximately 4 to 5 times larger than the structure length, as illustrated by the HAT empty graph in Fig. 5.3b.

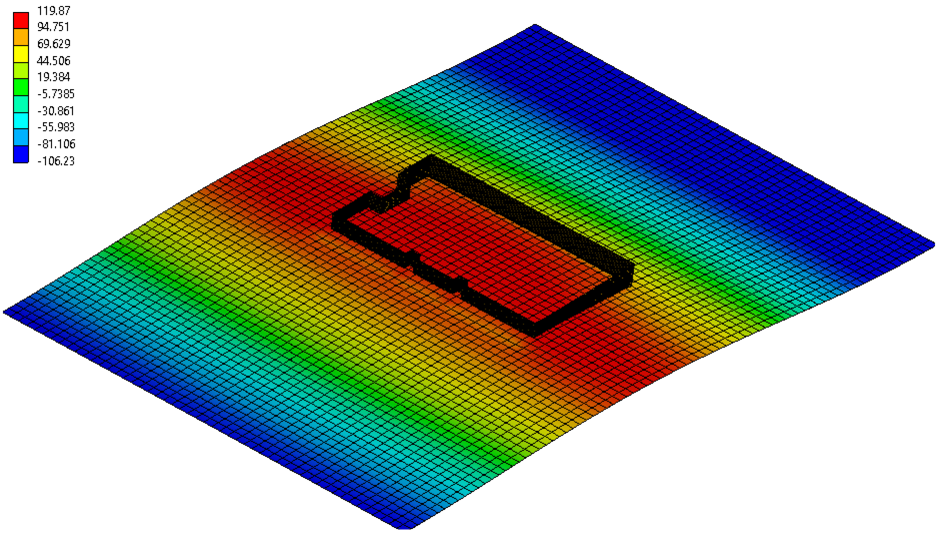

Figure 5.4: Visualization of wave surface elevation at heave peak in cm at HAT empty.

Fig. 5.5 visualizes the incident and diffracted heave force for different load cases at 180° waves.

A common observation is that generally, the LAT case attains a larger wave excitation effect. This is related to the larger wetted surface in the case of LAT. Furthermore, the graphs in Fig. 5.5 tends to grow with increasing wavelengths. This is in correlation with RAO curves in Fig. 5.3a and Fig. 5.3b.

It is worth being mentioned that the response of cases of HAT are larger, whereas in contrast, the wave excitation force in case of LAT is larger. This can be related to equation of motion 2.10, where with a smaller external force $\boldsymbol{F}$, as in the case of HAT, radiation effects decrease to maintain the higher peak response. Therefore, radiation effects are worth mentioning as well.

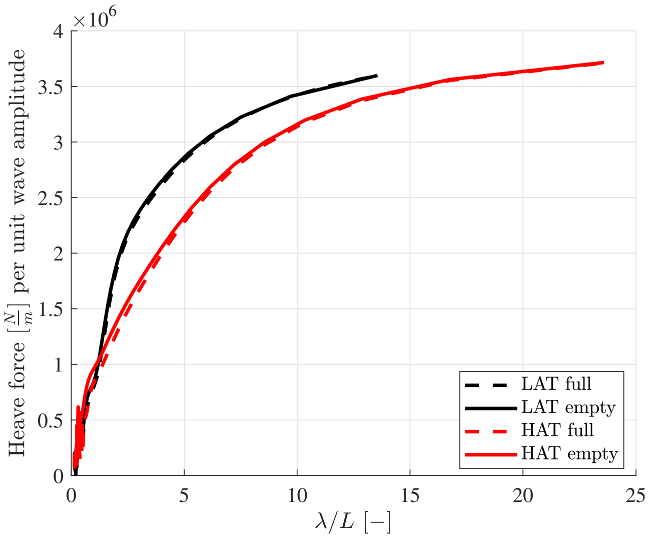

Figure 5.5: Visualization of incident and diffracted heave force for different load cases at 180° waves.

5.1.2 Roll

Fig. 5.6 shows the roll response for different wave cases due to 90° incident waves.

As depicted in Fig. 5.6, it can be seen that at the wave period around $T = 5$s, maximum response occurs. This corresponds to wavelength to structure length ratio in the range of 1 to 2 which is a smaller ratio than the case of heave in Fig. 5.3b despite the fact that the pontoon's breadth to length ratio is $b/L \approx 1.7$. In other words, although the pontoon is larger in y-direction than x-direction, smaller λ/L leads to maximum response.

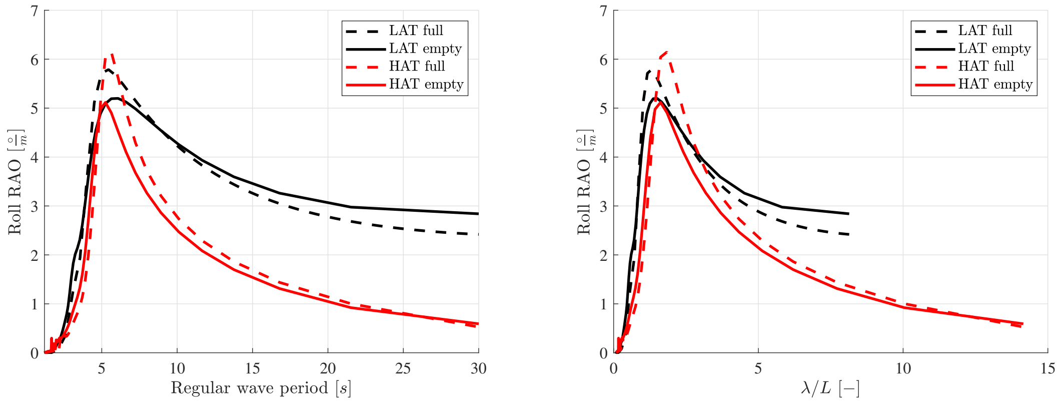

(a) Roll RAOs at different periods

(b) Roll RAOs at different λ/L

Figure 5.6: Visualization of roll response for different load cases at 90° waves. L is the breadth of the pontoon and λ the wavelength.

Wave excitation roll moments for the same load cases as in Fig. 5.6 are presented in Fig. 5.7. A direct observation is that in the case of LAT, wave moments are significantly larger than the case of HAT. This has to do with the higher angle of pitch which makes the draught larger in LAT. A larger wetted surface results in larger wave excitation moments, since these are a summation of surrounding hydrodynamic pressure distributions, as defined in Eq. 2.12. It is further observed that roll moment tends to decrease for increasing wavelengths. This can be related to larger periods, and consequently smaller frequencies.

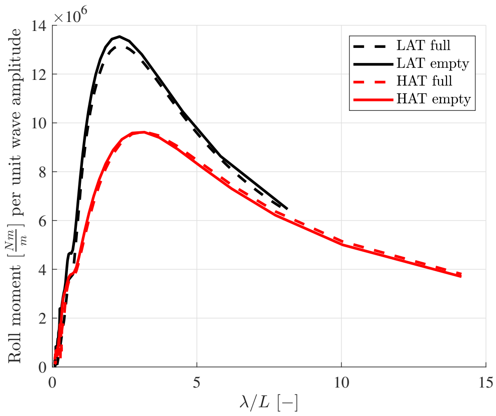

Figure 5.7: Visualization of incident and diffracted roll moment for different load cases at 90° waves.

Fig. 5.8 illustrates the LAT wave surface elevation for 90° peak response wave in case of empty and full. As shown by Fig. 5.6b, looking at the peak of the LAT graphs, near $\lambda/L \approx 1.5$, there is a peak response. This is also confirmed by Fig. 5.8. The magnitude of wave surface elevation is a function of incident wave amplitude, which is 1 m in this case.

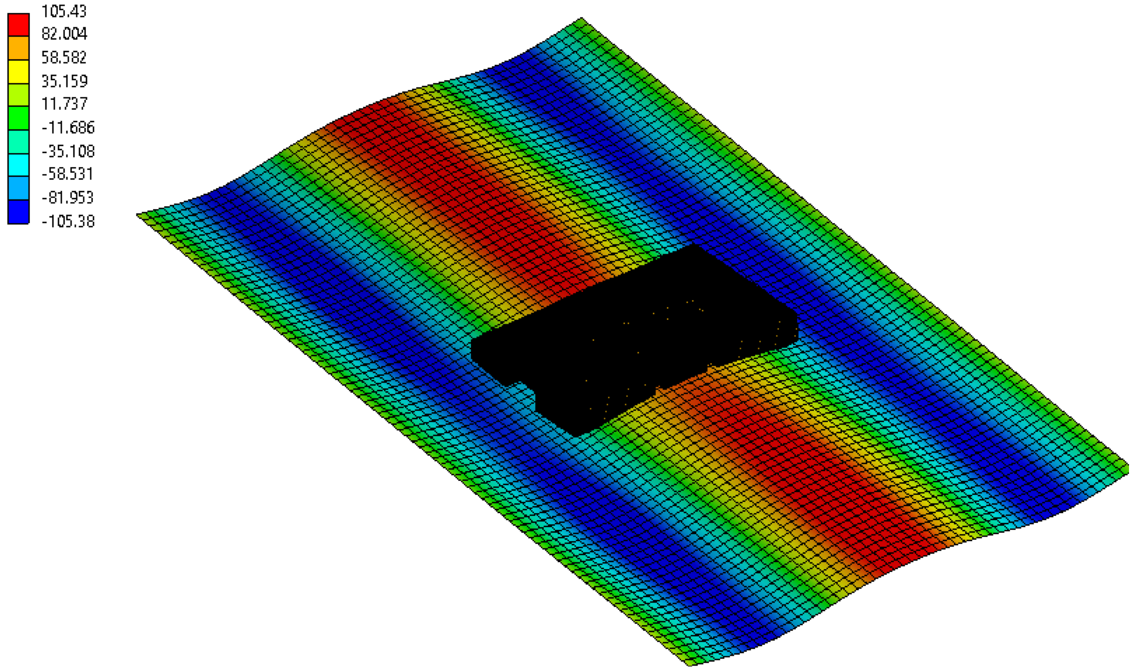

(a) Peak response wave for LAT full

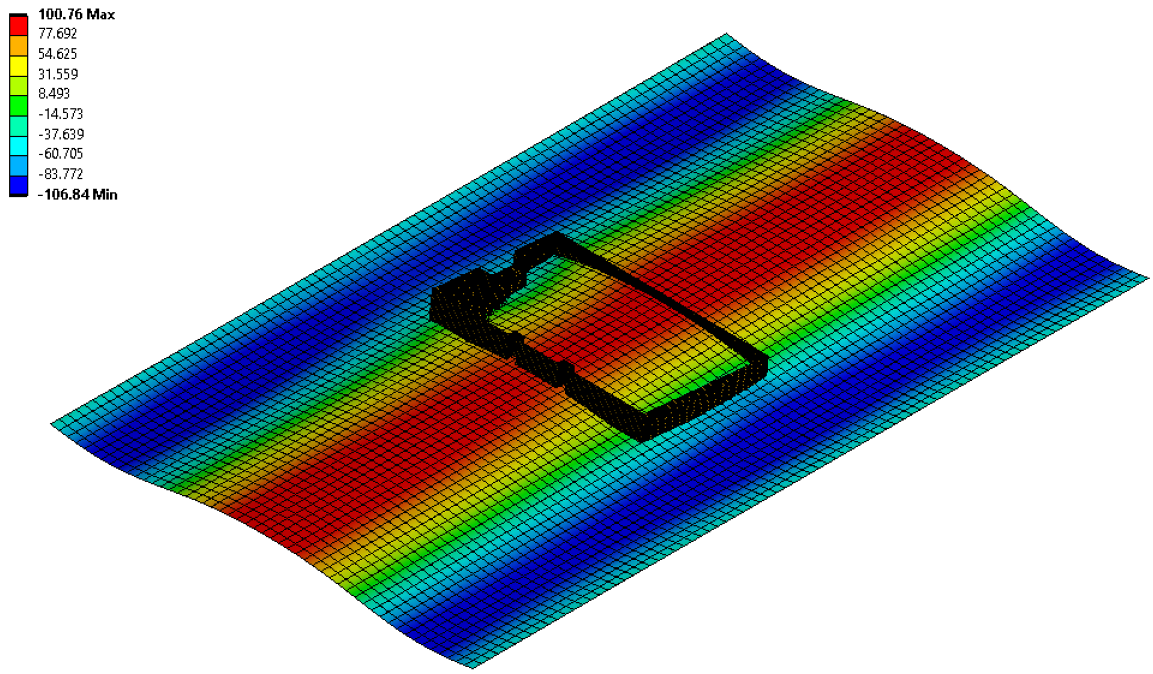

(b) Peak response wave for LAT empty

Figure 5.8: Visualization of wave surface elevation at roll resonance in cm.

5.1.3 Pitch

Fig. 5.9b and 5.9a show the pitch response. It can be seen that pitch response contains a number of peaks regardless of load case. At pitch, small wavelengths are clearly unstable for the structure. However, since the actual linkspan has other conditions according to Section 4.3.1, these enable the actual structure to be more stable against these peaks. It is evident that the response decreases with increasing wave period and wavelength, similarly to roll response in Fig. 5.6.

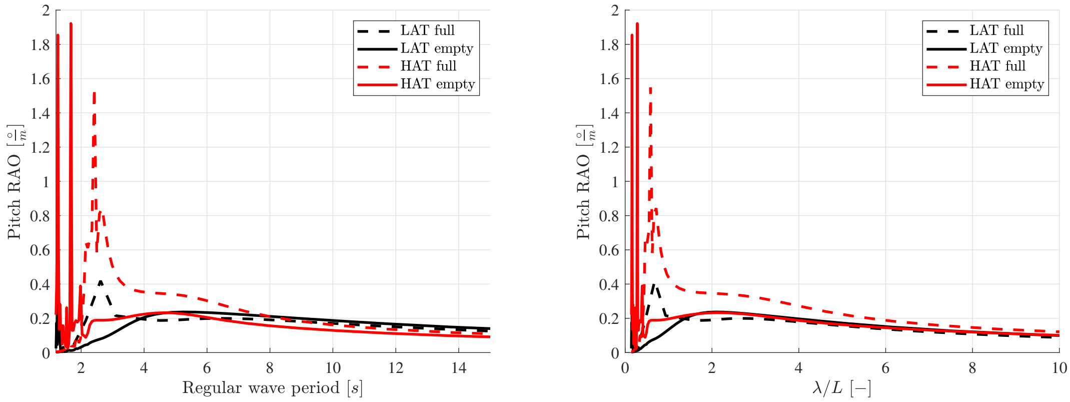

(a) Pitch RAOs at different periods

(b) Pitch RAOs at different λ/L

Figure 5.9: Zoomed visualization of pitch response for different load cases at 180° waves at peak areas. Here L is the length of the pontoon.

Figure 5.10 is showing pitch moment as a function of wavelength to structure length ratio. It can be observed that for all graphs in contrast to RAOs in Fig. 5.9b, for growing wavelengths, the pitch moment is growing as well. For the case of LAT full, the pitch moment is largest due to largest possible wetted surface.

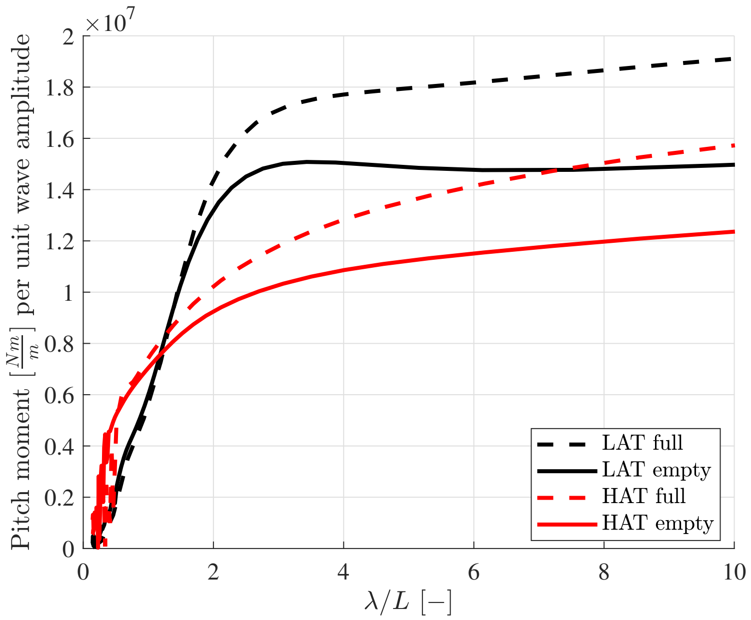

Figure 5.10: Visualization of incident and diffracted pitch moment for different load cases at 180° waves.

5.2 Flexible body analysis due to wave loads

In the upcoming sections, load mapping results are presented. As stated in Table 4.3, in the case of HAT, design wave 2 is mapped. This is a spectrum with return period of 100 years, significant wave height of 1.76 m and peak period of 4.19s. Correspondingly, in the case of LAT, design wave 1 is mapped. This is a spectrum with return period of 1 year, significant wave height of 1.22 m and peak period of 3.56s. The load mapping has been performed only for the empty cases.

The input parameters for AqwaWave was listed in Section 3.1.3.1. The input parameters that generated the maximum response in terms of directional deformation in z direction and equivalent (von-Mises) stress are presented in Table 5.1. Wave height for the individual waves are calculated by doubling the wave amplitudes. Wave amplitudes are obtained using Eq. 2.21 for the JONSWAP spectra shown in Fig. 4.7a.

Table 5.1: Input parameters that generated the maximum response

Load case	Wave phase angle [°]	Wave height [m]	Wave period [s]	Wave Direction
LAT	21.5	0.4	3.4	90°
LAT	169.6	0.4	3.7	180°
HAT	169.6	0.6	4.3	90°
HAT	169.6	0.6	4.3	180°

As earlier mentioned in Section 3.1.3.3, AqwaWave calculates the balancing accelerations based on the hydrodynamic model in terms of mass and inertia matrix information. The origin for balancing accelerations for the cases of HAT and LAT is shown by Fig. 5.11a and Fig. 5.11b respectively. This is the place where the fixed reference axis is located in the hydrodynamic model. Fixed reference axis is shown by Fig. 4.6 and discussed in Section 4.2.2.

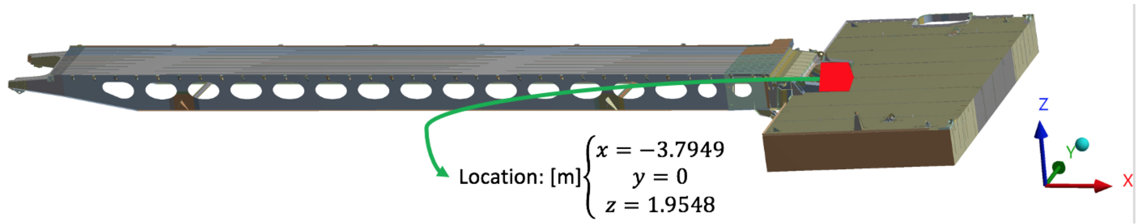

(a) HAT

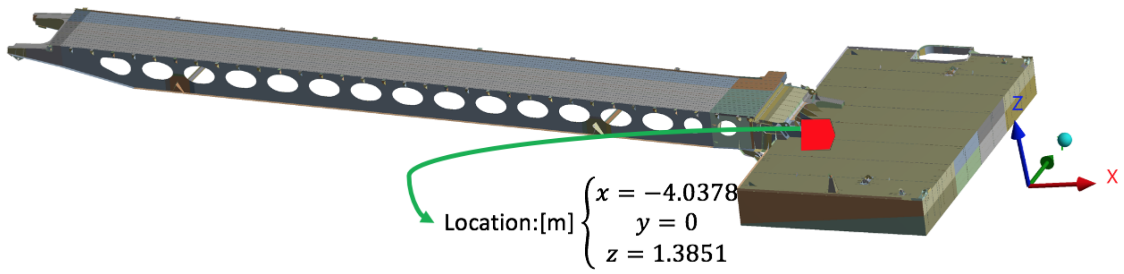

(b) LAT

Figure 5.11: Location for the origin of the acceleration coordinate system in the linkspan FE model.

5.2.1 Beam sea

The mapped balancing accelerations due to the beam sea waves for both cases is tabulated in tables Table 5.2 and Table 5.3. The origin for these is shown in Fig. 5.11.

Table 5.2: Linear accelerations at 90° waves.

Linear accelerations in m/s^2	a_x	a_y	a_z	$\mid \boldsymbol{a} \mid$
HAT	-0.0050	-0.0100	0.0810	0.0818
LAT	-0.0030	0.1490	0.0670	0.1634

Table 5.3: Angular accelerations at 90° waves.

Angular accelerations in rad/s^2	α_x	α_y	α_z	$\mid \boldsymbol{\alpha} \mid$
HAT	-0.0050	-0.0020	-0.0010	0.0055
LAT	-0.0110	-0.0020	0.0050	0.0122

Fig. 5.12 portrays the wave surface elevation at a particular phase angle, period and wave height, for which the load mapping is carried out. These parameters for each case are specified by Table 5.1. It can be seen that there is a wave crest at river side and middle of the pontoon, which causes the structure to rotate counterclockwise.

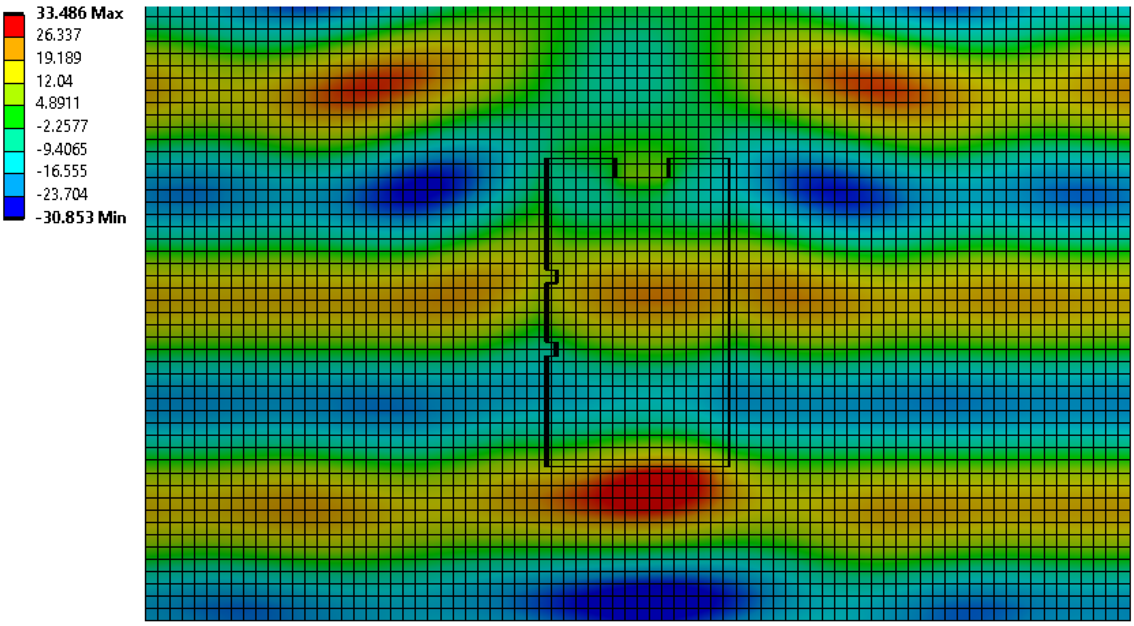

Figure 5.12: Wave surface elevation at the situation shown in 5.13 in cm.

Fig. 5.13 shows the stress results. Maximum equivalent stress is obtained at the hinge structure, which counteracts the torsion of the bridge due to the wave impact. However, it is still a very small maximum stress in both cases.

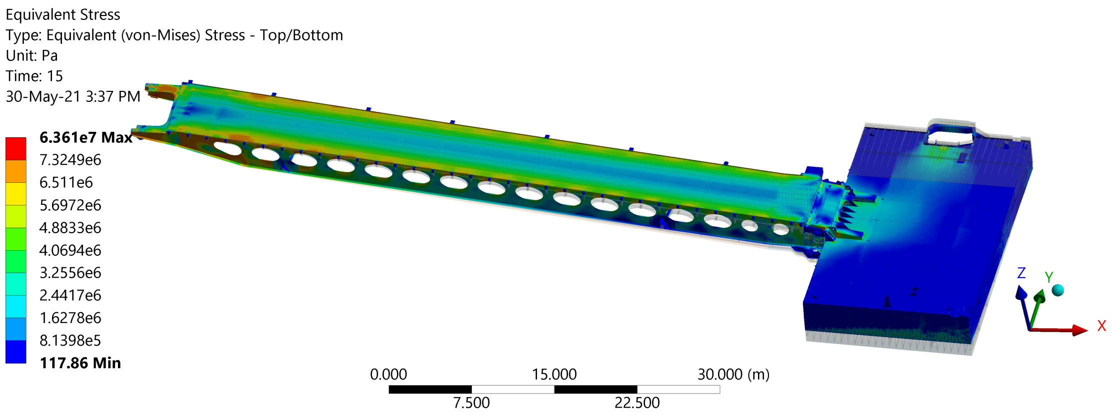

Figure 5.13: Maximum equivalent (von-Mises) stress results at LAT, subjected to beam sea for design wave 1 according to Table 4.2 occurs at a period of $T = 3.4s$.

Fig. 5.14 illustrates the deformation in z direction of the linkspan. It is clearly seen that there is a motion in upward direction on the river side, while the shore side goes down. This can be correlated to the wave surface elevation contour plot in Fig. 5.12, where there is a crest in the vicinity of the river side. See Fig. 4.1 for description of sides.

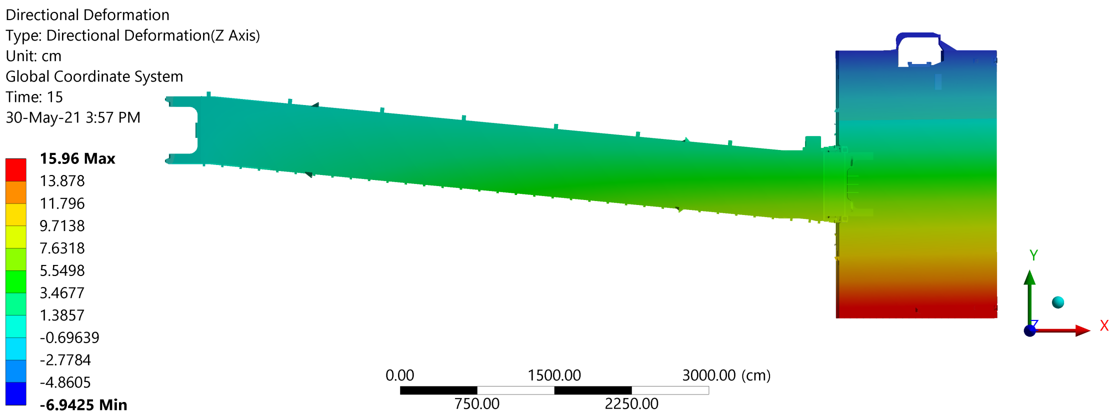

Figure 5.14: Deformation in Z direction in the same situation as figure 5.13.

Fig. 5.15 shows the wave surface elevation at the beam sea wave scenario, where the load mapping has been performed for HAT. This indicates that the pontoon is lying between two wave crests.

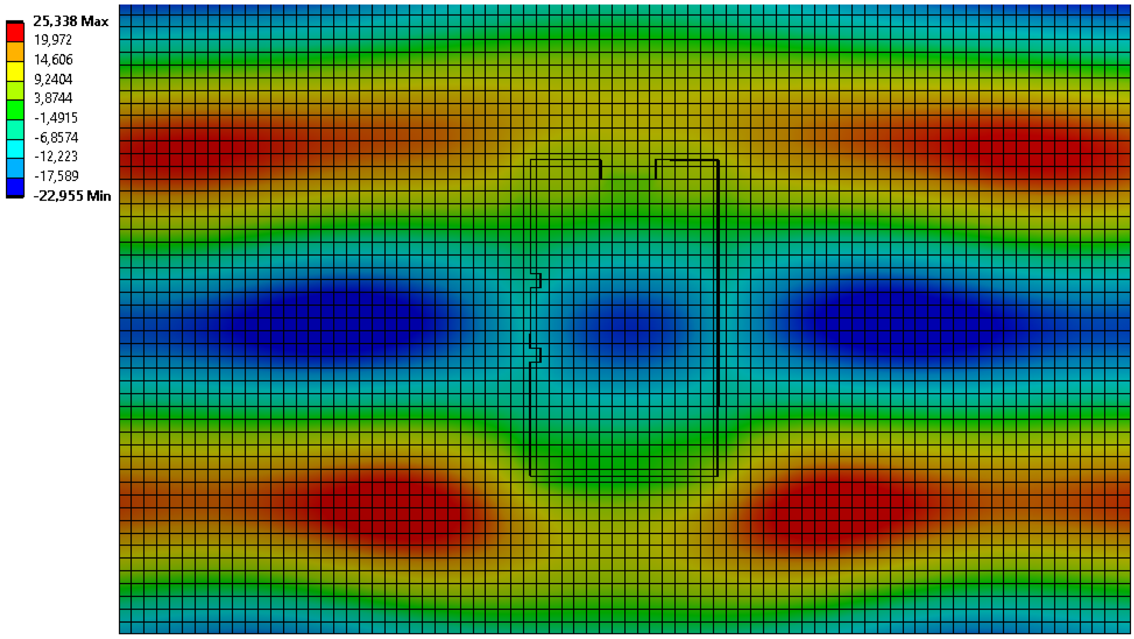

Figure 5.15: Wave surface elevation at the scenario shown in figure 5.16 in cm.

Fig. 5.16 illustrates the stress results for HAT subjected to beam sea waves for design wave 2 according to Table 4.2.

It can be seen that maximum stress in Fig. 5.16 is obtained at the hinge structure, here as well, since the torsion of the bridge is essentially taken up by the hinges. The torsion can be visualized in the directional deformation in z direction, as per Fig. 5.17.

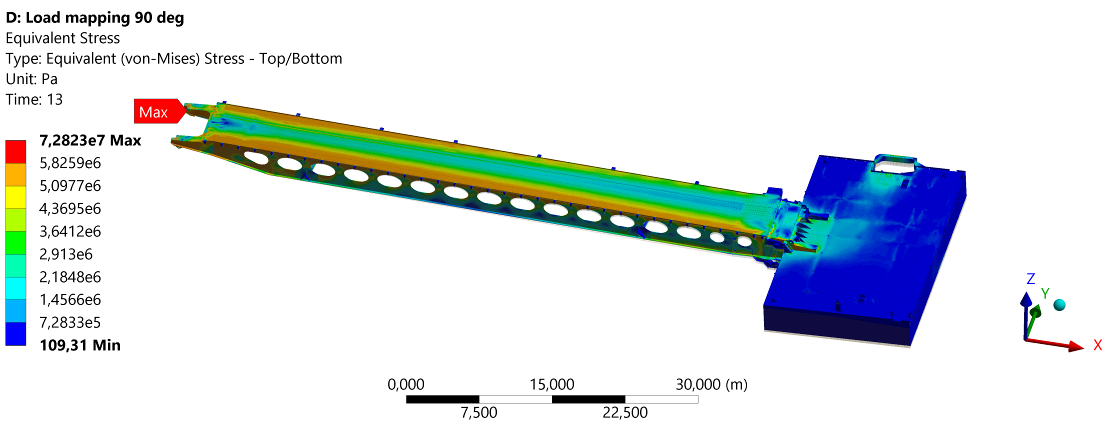

Figure 5.16: Maximum equivalent (von-Mises) stress results at HAT, subjected to beam sea for design wave 2 occurs at a period of $T = 4.3s$.

Fig. 5.17 is visualizing the directional deformation of the linkspan due to beam sea waves at HAT. This reflects the stress results obtained in Fig. 5.23, where a counterclockwise direction around x axis is occurring.

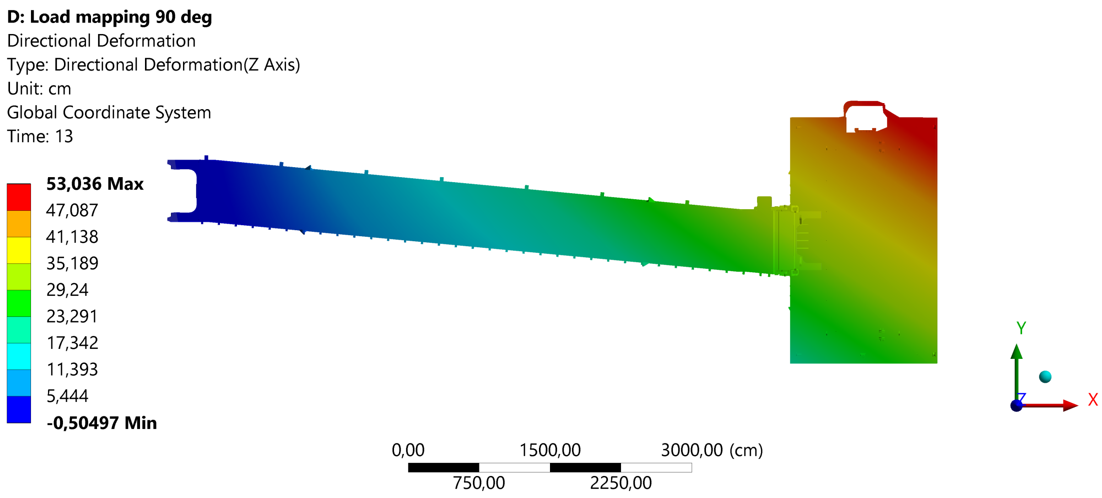

Figure 5.17: Deformation in z direction in the same scenario as figure 5.16.

5.2.2 Inertial relief

Compared to Fig. 5.17, where weak springs solver control was employed, Fig. 5.18 illustrates the directional deformation field where inertial relief option is instead employed. It is clearly noticeable that deformations are by order of 20 smaller. This can be seen as an indication that the simulations performed using weak springs option, where in contradictory it follows the hydrodynamic model, are over-predicting the wave impact. In other words, there is a difference in pre-defined inertia in the hydrodynamic model in Aqwa according to tables Table 4.4, Table 4.4, Table 4.5 and calculated inertia for the structural model by Ansys Mechanical. Inertial relief option is following the structural model's mass and inertia matrix information when calculating the balancing accelerations.

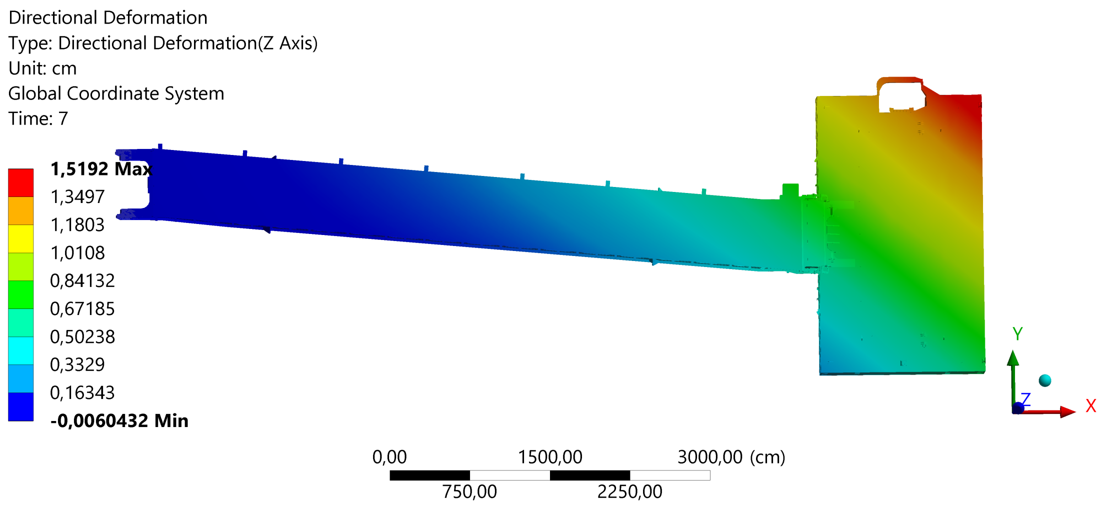

Figure 5.18: Deformation result for inertial relief condition at HAT

5.2.3 Head sea

As a result of load mapping, the balancing linear and balancing angular acceleration vectors are calculated by AqwaWave. These are presented in tables 5.4 and 5.5 respectively. At HAT, accelerations are calculated at the wave scenario shown by Fig. 5.22. The corresponding wave scenario for LAT is illustrated by Fig. 5.19.

One significant observation is that the balancing acceleration vectors are by magnitude larger in HAT than LAT, as shown in tables 5.4 and 5.5. This can be related to the contour plot in Fig. 5.22, where in this case the pontoon is located between two crests in a worse wave scenario.

Linear accelerations in m/s^2	a_x	a_y	a_z	$\mid \boldsymbol{a} \mid$
HAT	0.1040	-0.0020	0.2290	0.2515
LAT	-0.1340	0.0040	0.0300	0.0054

Table 5.4: Balancing linear accelerations at 180° waves.

Angular accelerations in rad/s^2	α_x	α_y	α_z	$\mid \boldsymbol{\alpha} \mid$
HAT	0	-0.0370	0	0.0370
LAT	-0.1340	0.0040	0.0300	0.1374

Table 5.5: Balancing angular accelerations at 180° waves.

Wave surface elevation as per Fig. 5.19, reflects the present wave scenario at the particular mapped wave in Fig. 5.20. It can be seen that the pontoon (hydrodynamic model) is facing a wave crest. This causes a large deformation in z direction, as seen in Fig. 5.21.

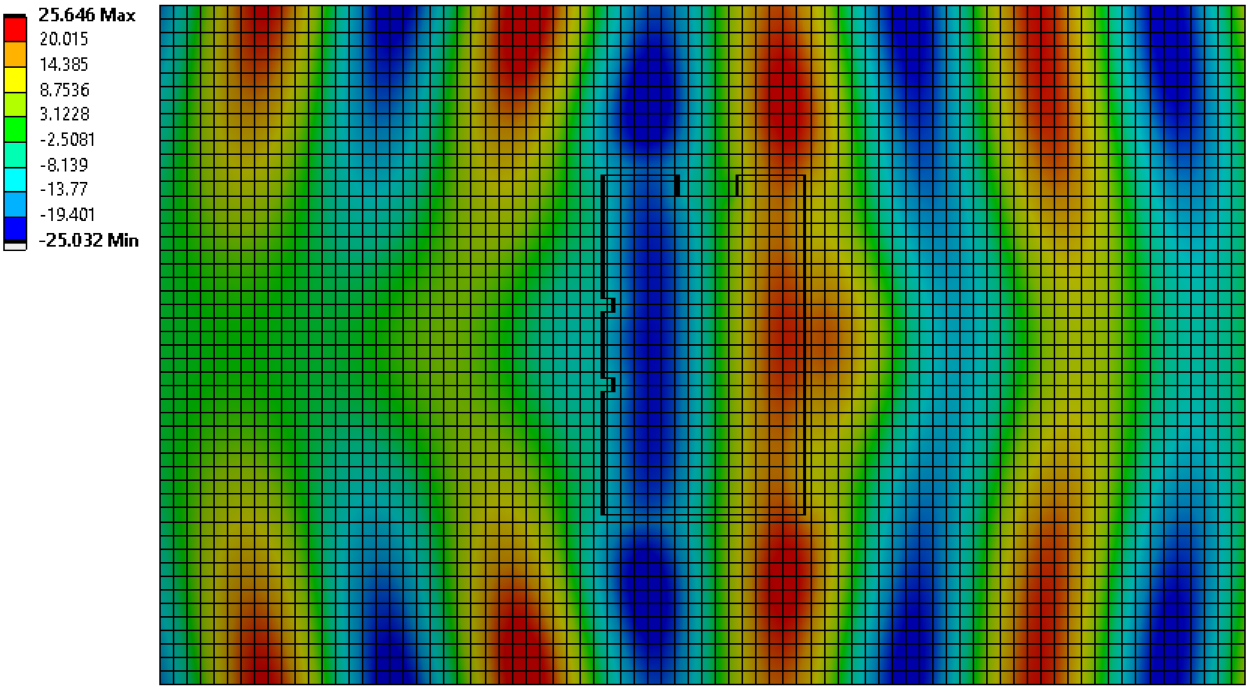

Figure 5.19: Wave surface elevation at the situation shown in figure 5.20 in cm.

Fig. 5.20 illustrates the equivalent (von-Mises) stress results at LAT, for the wave scenario that is shown in Fig. 5.19. The structure senses the stress the hinge part mostly, since it is prevented from translation in x direction.

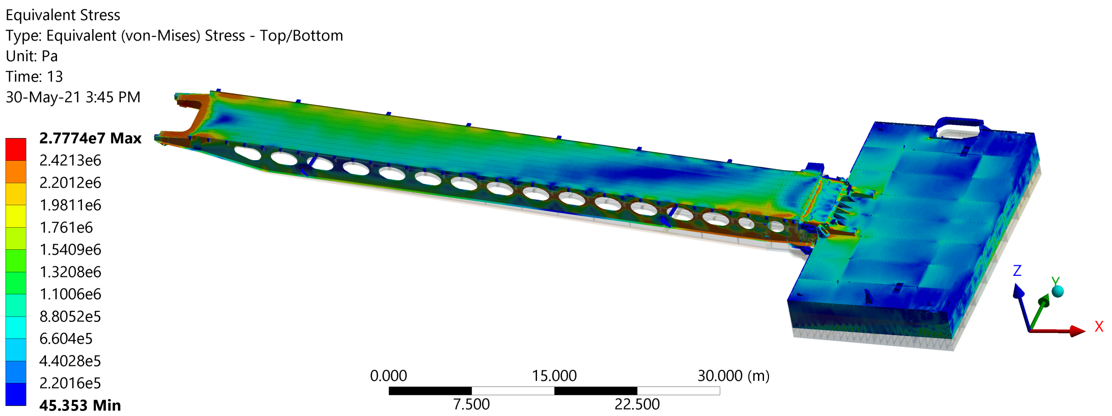

Figure 5.20: Maximum equivalent (von-Mises) stress results at LAT, subjected to head sea for design wave 1 occurs at a period of $T = 3.7s$.

Deformation in Fig. 5.21 reflects the behavior of the structure when influenced by the wave impact, portrayed in Fig. 5.19. The structure is deformed more on the shore side. This can be related to the unsymmetrical nature of the geometry.

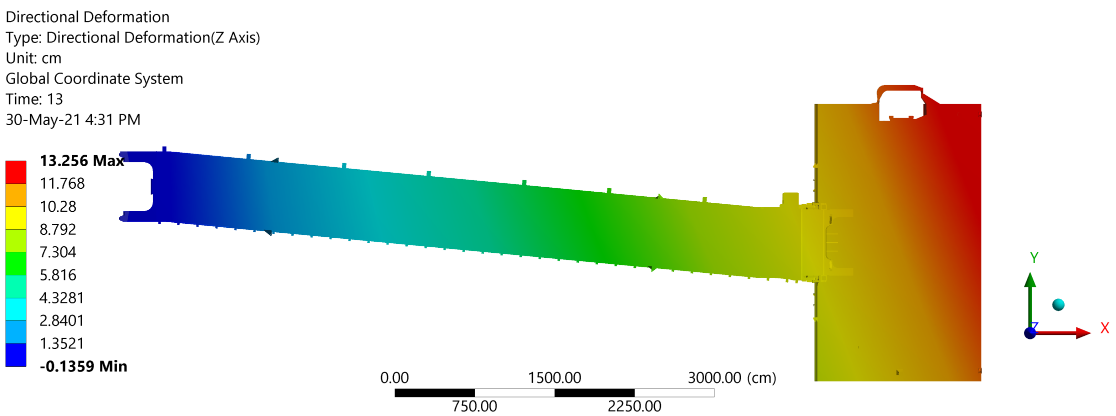

Figure 5.21: Deformation in z direction in the same situation as figure 5.20

Wave surface elevation as per Fig. 5.22 reflects the present wave scenario at the particular mapped wave in Fig. 5.23 at HAT. It can be seen that the pontoon is facing a large wave crest from front at this particular phase.

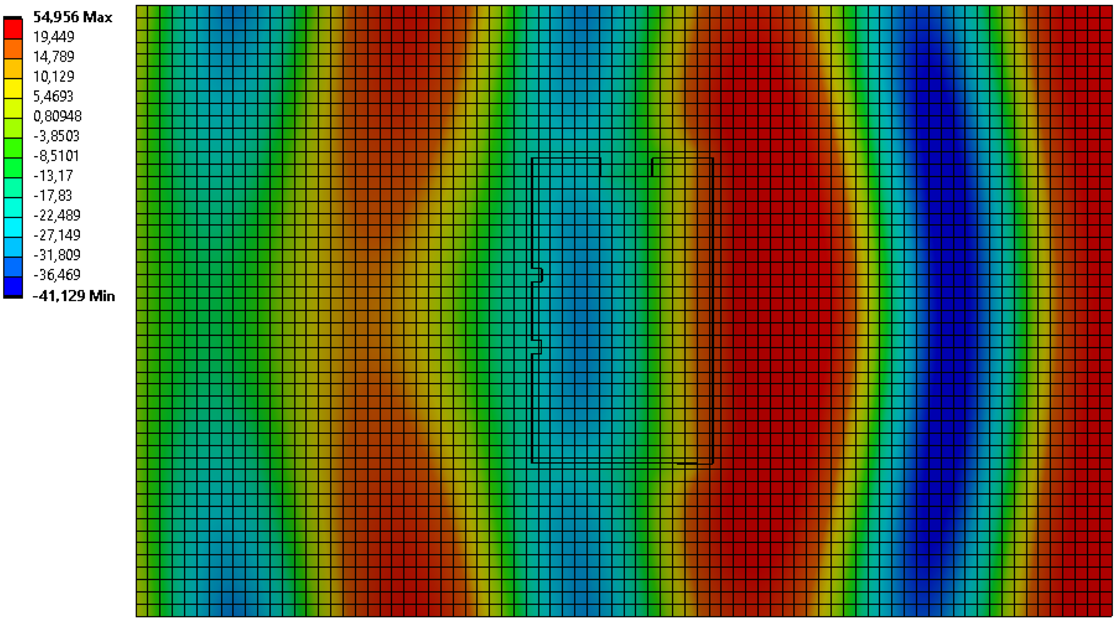

Figure 5.22: Wave surface elevation at the situation shown in figure 5.20 in cm.

Fig. 5.23 portrays the maximum stress results. The stress results is clearly reflecting the deformation in Fig. 5.24.

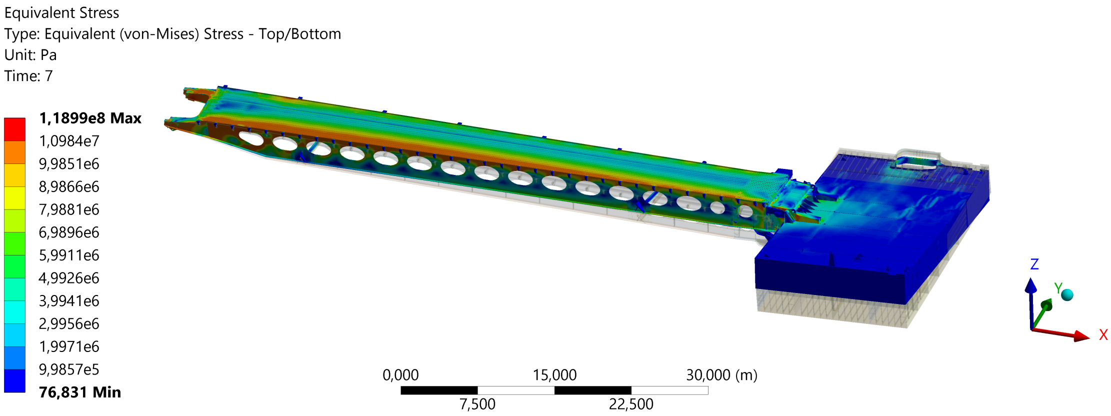

Figure 5.23: Maximum equivalent (von-Mises) stress results at HAT, subjected to head sea for design wave 2 occurs at a period of $T = 4.3s$.

By comparing Fig. 5.24 and Fig. 5.22 it is shown how the structure responds to the incident wave in terms of deformation in z direction. Since the structure in not symmetric the head sea wave seems not have the same effect on the linkspan structure than it has on the free floating body. This is an effect of the higher level of details that are present in the FE model, which adds complications to the analysis.

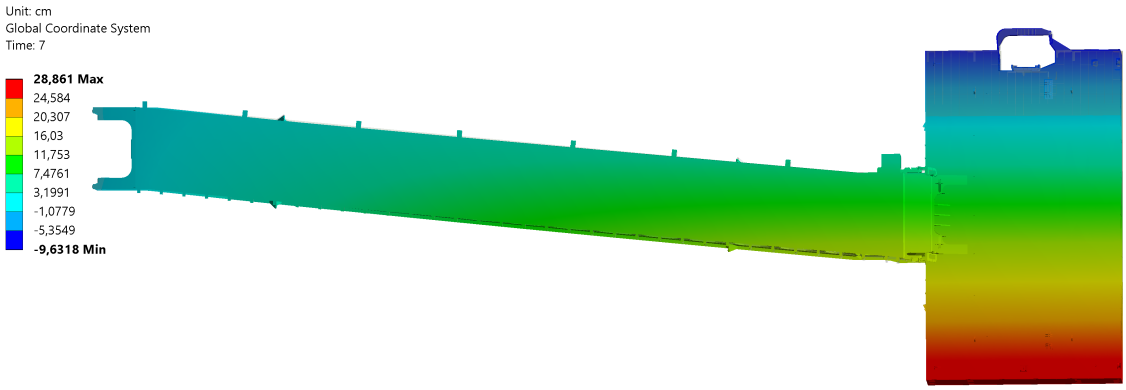

Figure 5.24: Deformation in Z direction in the same situation as figure 5.23

5.2.3.1 Inertial relief

Fig. 5.25 illustrates a contour plot of deformation in z direction of the model which is significantly smaller in relation to computed version by weak springs solver control, as Fig. 5.24 shows. This can be interpreted, similar to results for beam sea in Fig. 5.18 as an indication that the calculated inertial loading in terms of balancing accelerations in table 5.4 and 5.5 are over-predicting the external pressure force and that there is a difference between the structural model and the hydrodynamic model in terms of inertia.

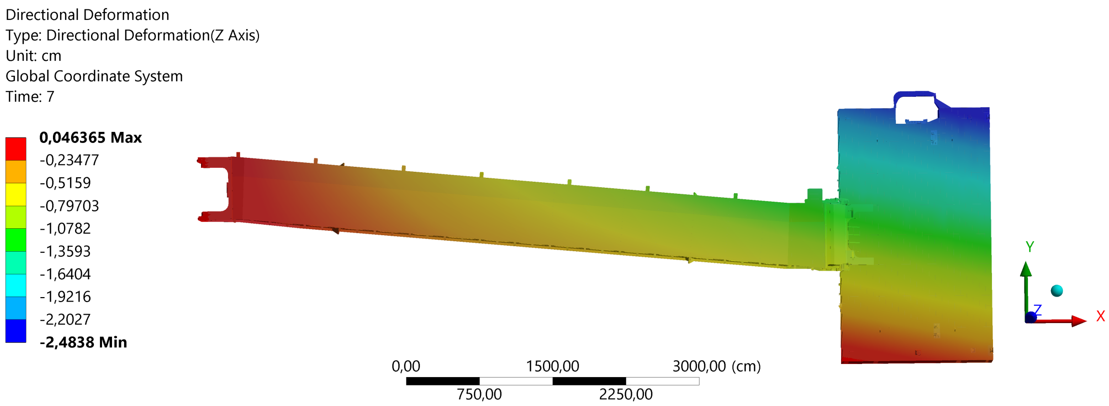

Figure 5.25: Results from inertial relief constraint for HAT case.

5.3 Discussion

As Fig. 4.2 showed, two types of interval definitions were conducted in this thesis. By observing the hydrodynamic graphs, almost all of them has shown that at smaller wave periods there is a need for having a fine mesh when solving the hydrodynamic problem, since this is when the peak response occurs. For the case of roll and heave, the period interval of 5-10s has shown peak responses. By observing Fig. 4.2a and Fig. 4.2b it is seen that for example for the case of pitch in Fig. 5.9a the configuration in Fig. 4.2a is a better approach since it is at the peak response region Fig. 4.2a have a finer interval definition. In the case of roll, as per the RAO curves in Fig. 5.6a, it can be seen that the period based interval, as in case of Fig. 4.2b provides a better division of the peak response period interval. Nevertheless, the overall behaviour of the RAO curves looks similar despite the different interval definitions. A more optimized way of definition is probably a combination of both Fig. 4.2a and Fig. 4.2b. Practically, this can be accomplished by dividing the whole interval, and run simulations with period based approach for a certain interval where for example a finer mesh is sought and for the rest the uniform option according to Fig. 4.2b can be used. To obtain a good first approximation, it is however better to go with 4.2b and combine thereafter with a good judgement.

As stated in AqwaWave's manual, elements in the FE model generally do not correspond to the elements in the Aqwa model. This is true in this thesis project as well. Furthermore, the wetted surface that has been defined for the load mapping does not correspond exactly to the wetted surface that is actually considered by Aqwa solver. The asas file contained the whole pontoon model (panel model), whereas in Aqwa the submerged part, as shown in Fig. 4.8 is only considered in the analysis. Thereby, a number of warnings related to this have been obtained during the load mapping, which was due to excessive interpolation, as explained in Fig. 3.4. It was however observed from stress contours that the distribution of panel pressures were applied correctly since the water line could be seen, if the colorbar was sufficiently adjusted.

A further common observation for the stress contour plots is worth mentioning. The maximum von-Mises stress is small, which depends on the wave amplitudes that are small as well, as it was illustrated by Fig. 4.7b.

Since there is a difference between structural geometry and hydrodynamic geometry, inertial loads may not be in exact balance with pressure loads. Thereby, this can affect the trustworthiness of the actual result, which leaves space for improvement and development of the current approach.

Ideally, it would be better to be able to carry out hydrodynamic analysis of the whole linkspan model. This cannot be afforded due to limitation in the Aqwa solver in terms of diffracting and total element number. Furthermore, the actual linkspan model contains a lot of geometry complications which is not appreciated by Aqwa solver. Therefore, in this thesis the pontoon par was chosen.

Another improvement could be that inertial relief option could be explored more. This requires that the hydrodynamic model and the structural FE model should have the same CoG, which was not the case, related to the issue addressed in the previous paragraph. Despite this issue, the inertial relief option seemed to work, despite that it might not have been the ideal way of use. The inertial relief option was accomplished by not considering the mapped accelerations, contradictory to when the weak springs option was used.

When choosing wetted surface, as mentioned in Section 3.1.3.2, it can be a good idea to reconsider the choice of wetted surface to which the mapped pressures will apply. This was not easily doable and splitting edges could result in damaging the geometry file. Therefore in case of future work, it is good to include the aspect of wetted surface and load cases in an earlier phase of design process, namely when building the model from scratch, the wetted surface can be kept in mind.

In this thesis, hydrodynamic simulations that have been carried out are using linear airy theory. This a sufficient theory to model the physics of this problem, since no second order terms related to drift is necessary for stationary structures as linkspan.

As a validation, results have been compared with Wamit analyses that are done before, and findings were correlating, especially the wave forces. This can be considered as a validation for the results in the hydrodynamic part.

For the load mapping part, it has not been easy to validate. Since this case study has not been covered anywhere else it has been difficult to obtain a good validation. Performing own testing has not either been possible since most of the time for the work has been put to explore the possibility to carry out such simulations. It is therefore important, in case of future work, to have the validation step in mind to ensure that the results obtained are free from errors and model the physics sufficiently correct.

6
Conclusion

Heave response at HAT cases attain a larger value at the period interval of 5-15s. For all cases, it can be seen that after the peak wavelength, the response becomes eventually constant. The excitation forces in heave looks a little different. The graphs tend to grow with increasing wavelength, although with a smaller rate towards $\lambda/L \approx 10$. LAT has a slightly larger wave excitation force than HAT, which can be related to larger wetted surface.

When it comes to roll response, the peak is obtained in the vicinity of the same period as for heave, but this corresponds to a much smaller λ/L i.e. when wavelength λ is closer to structure length L. In this sense, the structure is stiffer in head sea (heave and pitch) than beam sea (roll). Similar to heave excitation force, roll excitation moment is larger in the case of LAT. Roll response and roll excitation moment decrease after their respective peak.

Pitch response is critical at smaller wavelengths at HAT. The response tends to decrease for larger wavelengths and periods. Wave excitation effects are generally larger for LAT case.

A common conclusion from the load mapping part is that the maximum stress is obtained at the hinge structure. Load mapping Load mapping is a good tool to use to understand wave influence on structural strength, however it requires improvements. As an example, structural and hydrodynamic model should have matching inertia in order to obtain a more proper load mapping. It is good to find a validation for this part to ensure that the results are free from errors.

For a future work, it is good idea to try to have the same geometry in the FE model and the hydrodynamic model. Hydrodynamic model should have same CoG as structural model. It was however not possible in this thesis because that would require higher level of detail than the capacity of Aqwa. Since inertial relief seemed to give more realistic results, it is good to check this approach towards the classification rules before proceeding to use it in real-life projects. It can also be a proper future work to expand the load mapping approach for fully loaded condition to understand stability aspects more.

References

ANSYS Inc. (2013a). ANSYS Mechanical APDL verification manual [Computer software manual]. Canonsburg, T.D..

ANSYS Inc. (2013b). *Load Mapping.* `https://dokumen.tips/documents/aqwa-intro-14-5-ws05-1-load-mapping.html`. (Accessed: 2018-05-18)

ANSYS Inc. (2021a). Aqwa theory manual [Computer software manual]. Canonsburg, The US..

ANSYS Inc. (2021b). Aqwawave manual [Computer software manual]. Canonsburg, The US..

BSI. (2007). *Maritime structures – part 8: Code of practice for the design of ro-ro ramps, linkspans and walkways* (Tech. Rep. No. BS 6349-8:2007). 389 Chiswick High Road London W4 4AL United Kingdom: The British Standards Institution.

Carl-Erik Janson. (2015). *Lecture notes for sjo 745 wave loads and seakeeping.* `https://chalmers.instructure.com/courses/9398`. (CHALMERS UNIVERSITY OF TECHNOLOGY Gothenburg, Sweden 2015-03-18)

Chamberlain, N. (2020, February). *Isle of Man Ferry Terminal, Summary of Wave Modelling* (Tech. Rep. No. PB8850-RHD-ZZ-XX-RP-C-0003). Liverpool, UK: HASKONINGDHV UK LTD.

Det Norske Veritas. (2010). *Environmental conditions and environmental loads.* `https://rules.dnv.com/docs/pdf/DNVPM/codes/docs/2010-10/rp-c205.pdf`. (Accessed: 2021-05-16)

DfT. (2020). *Uk Port Freight Statistics: 2019.* `https://assets.publishing.service.gov.uk/government/uploads/system/uploads/attachment_data/file/908558/port-freight-statistics-2019.pdf`. (Accessed: 2021-05-12)

Gabriel Ruiz Martinez. (2021). *Dispersion relationship for water waves.* `https://se.mathworks.com/matlabcentral/fileexchange/23995-dispersion-relationship-for-water-waves`. (Retrieved: May 21, 2021)

Ibinabo, I., & Tamunodukobipi, D. T. (2019). Determination of the Response Amplitude Operator(s) of an FPSO. *Engineering*(11), 541–556.

Ji, J., Kim, K., Seo, M., Kim, T., Park, D., Kim, Y., & Ko, K. H. (2014). Load mapping for seamless interface between hydrodynamics and structural analyses. *Advances in Engineering Software*, *71*, 9–18.

Le Méhauté, B. (2013). *An introduction to hydrodynamics and water waves.* Springer Science & Business Media.

Malm Gustafsson, K. (2021). *Comments from supervisor.*

Masoudi, E., & Zeraatgar, H. (2017). Hydrodynamic analysis of various cross sections of floating breakwaters. In *Proceedings of 7th international offshore industries conference (sharif university of technology, tehran, iran)* (p. 82).

Osborn, S. (2010). The design of ship-to-shore linkspans for ro-ro terminals. In *Proceedings of the institution of civil engineers-civil engineering* (Vol. 163, pp. 34–40).

UNCTAD. (2018). *Review of Maritime Transport 2018.* `https://unctad.org/webflyer/review-maritime-transport-2018`. (Accessed: 2021-05-19)

Wallnöfer, T. (2015, 6). *Form Hydrodynamic Loading to Global Strength Assessment of Offshore Vessels.* `http://www.cae-wiki.info/wikiplus/images/9/9f/UM2015-2.01.02.pdf`. (Accessed: 2021-05-15)

Xu, H., Neng, P., & Yang, F. (2019). Motion response analysis of mining vessel based on ansys/aqwa. In *Journal of physics: Conference series* (Vol. 1300, p. 012010).

A

Appendix A

A.1 Input Data file

According to below the input data file used in AqwaWave is placed below (ANSYS Inc., 2013b).

```
* Standard lines for ASAS style data:
SYSTEM DATA AREA 5000000
JOB NEW LINE
PROJECT ANSY *At present ANSYS files default to project ANSY
* Extension of the output files (*.txt)
EXTENSION txt
END
* Define structural model
* (in this case output from anstoasas command)
stru asas file.asas
* Define hydrodynamic model
hydr aqwa analysis
END
AQWAID
* Following commands set target structural
* analysis system as ANSYS Mechanical
FELM
FEPG ANSYS
END
LOAD
* Load information
* Case Current_ID Frequency_ID Direction_ID Wave_Height Phase
END
*Stop processing this file.
STOP
```

B
Appendix B

B.1 RAOs

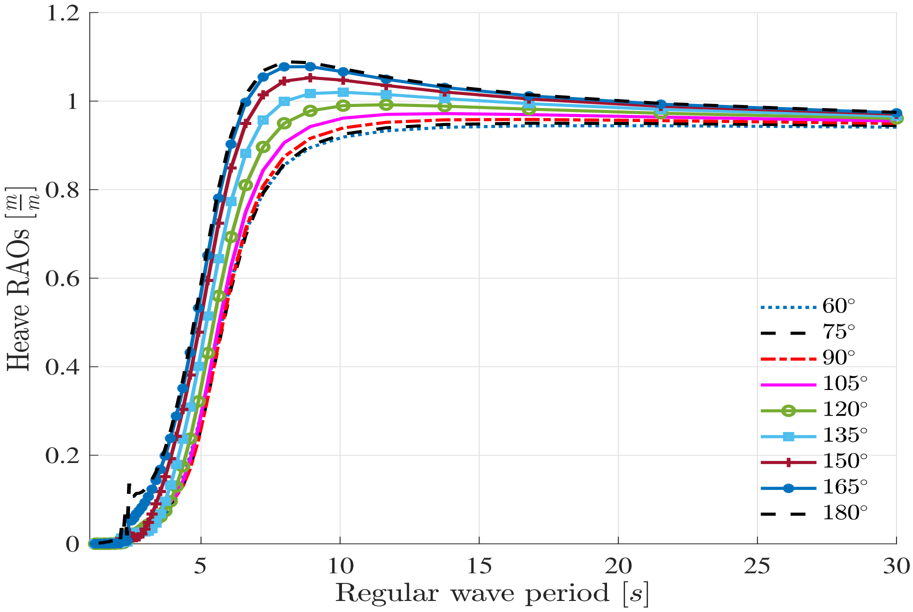

(a) Heave RAOs at different directions for case HAT full.

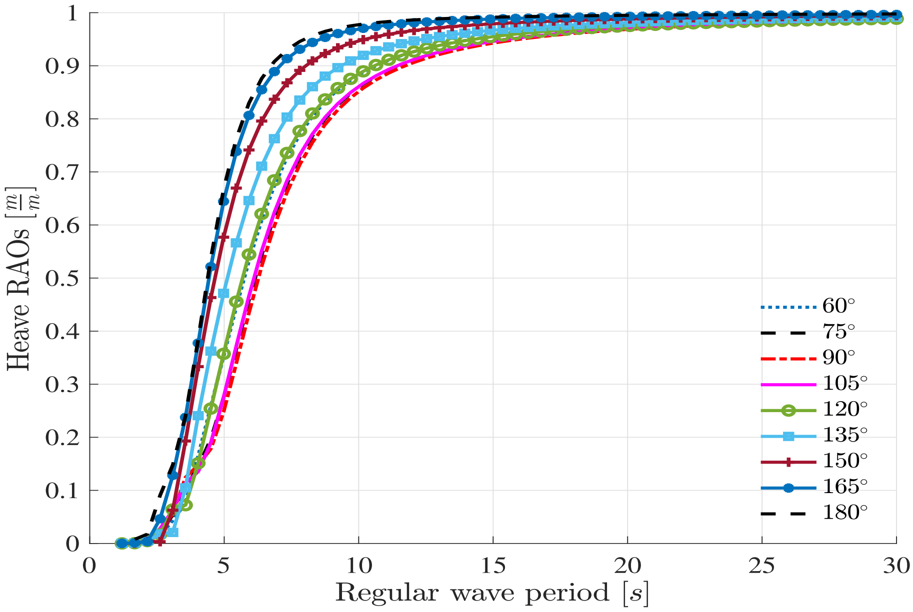

(b) Haeve RAOs at different directions for case LAT full

Figure B.1: Visualization of heave response for different load cases at 60° → 180° waves angles.

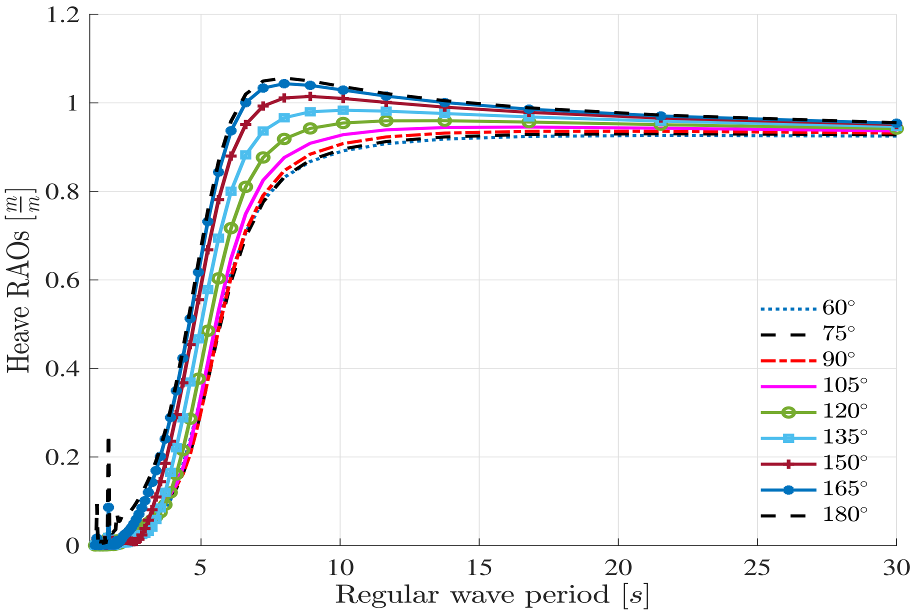

(a) Heave RAOs at different directions for case HAT empty.

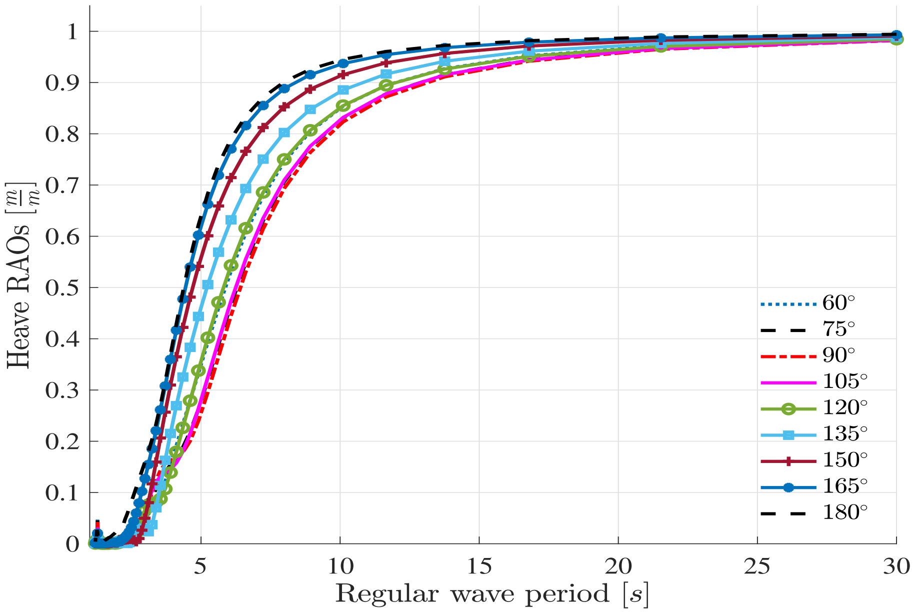

(b) Haeve RAOs at different directions for case LAT empty.

Figure B.2: Visualization of heave response for different load cases at 60° → 180° waves angles.

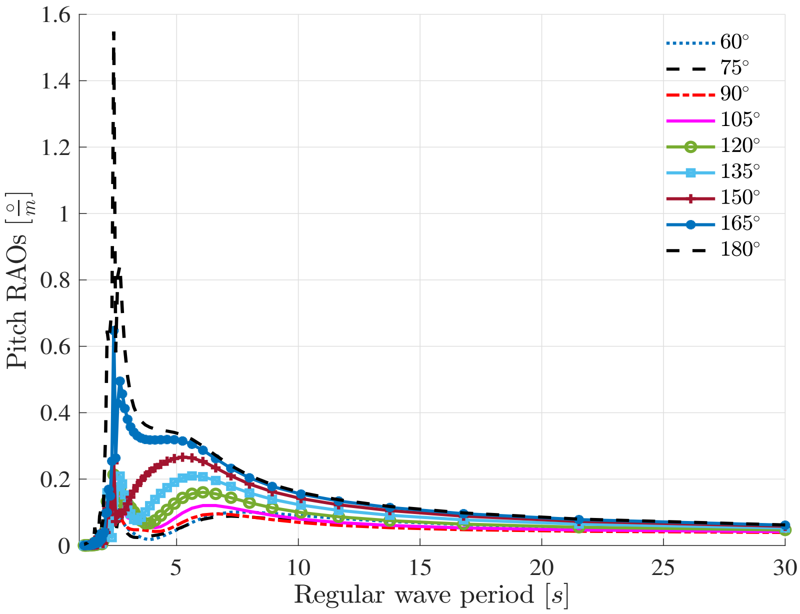

(a) Pitch RAOs at different directions for case HAT full.

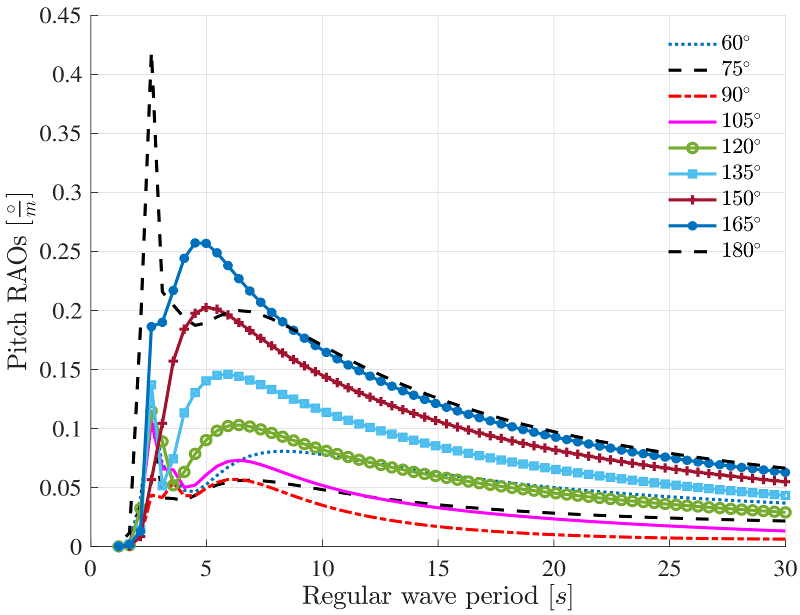

(b) Pitch RAOs at different directions for case HAT full.

Figure B.3: Visualization of pitch response for different load cases at 60° → 180° waves angles.

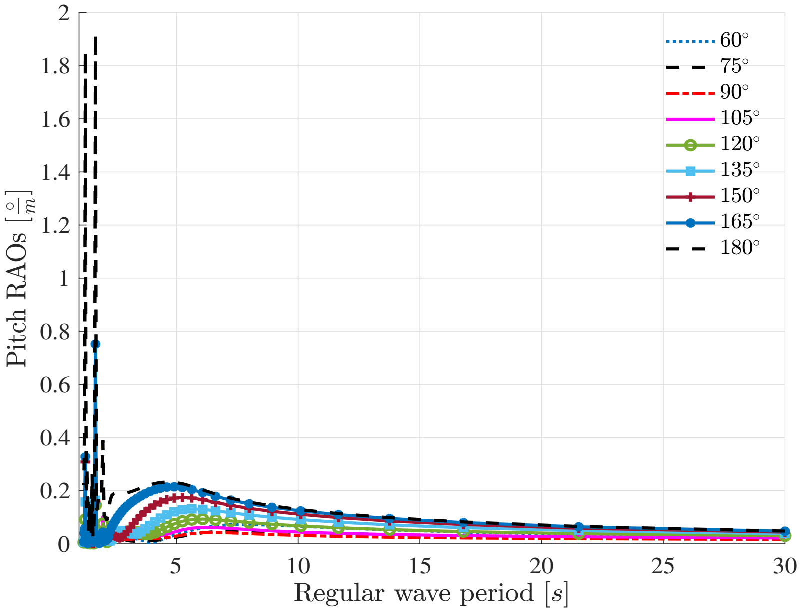

(a) Pitch RAOs at different directions for case HAT empty.

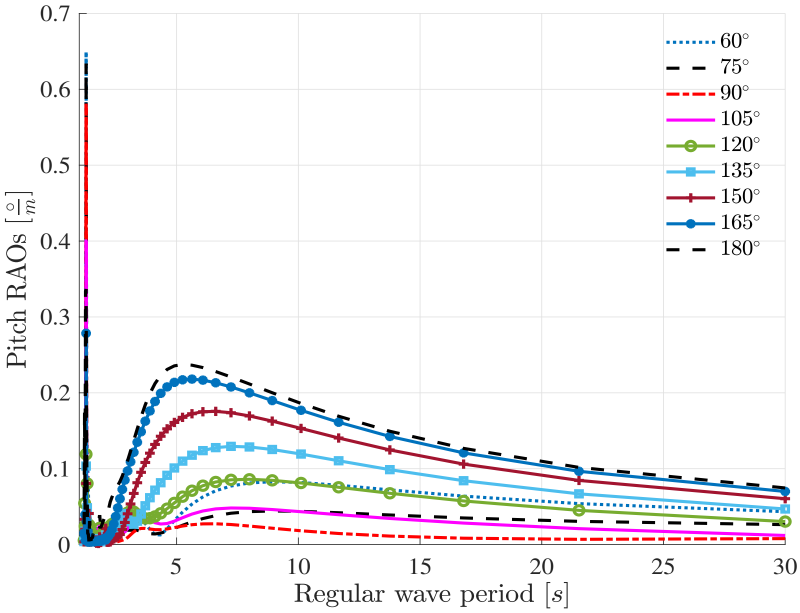

(b) Pitch RAOs at different directions for case HAT empty.

Figure B.4: Visualization of pitch response for different load cases at 60° → 180° waves angles.

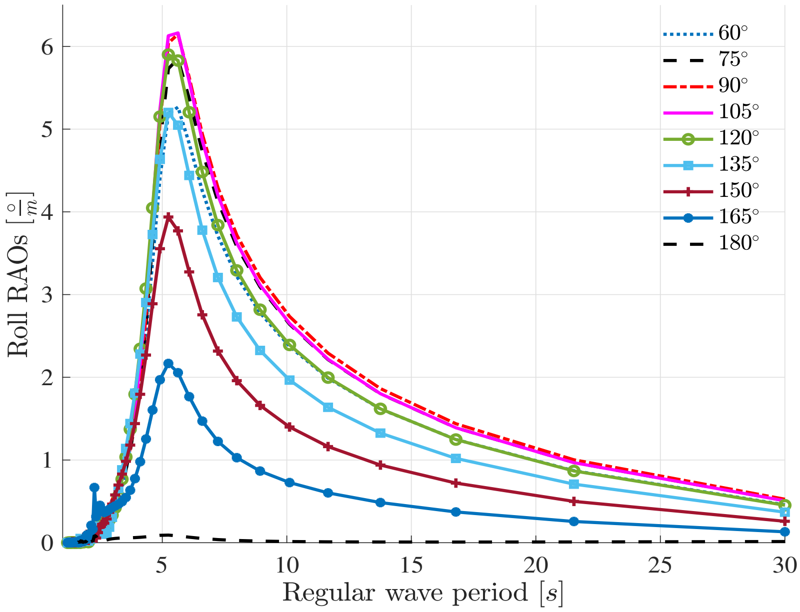

(a) Roll RAOs at different directions for case HAT full.

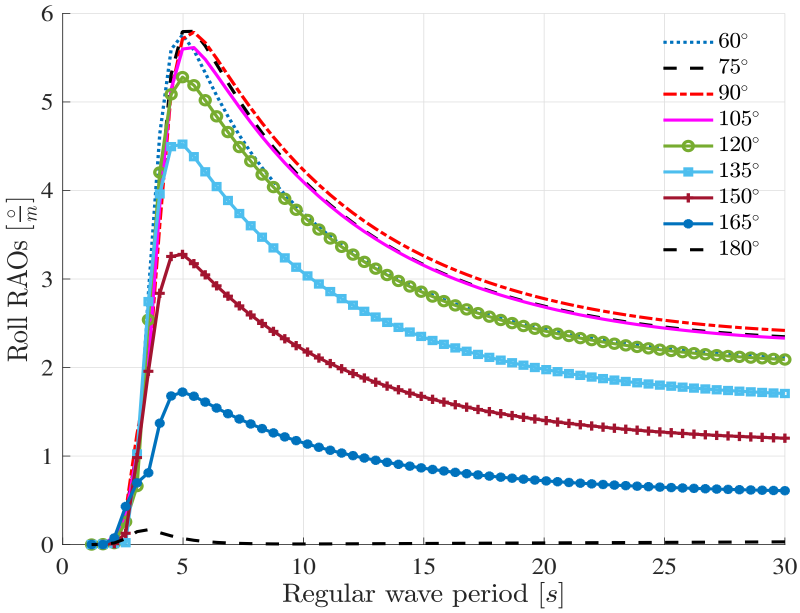

(b) Roll RAOs at different directions for case LAT full.

Figure B.5: Visualization of roll response for different load cases at 60° → 180° waves angles.

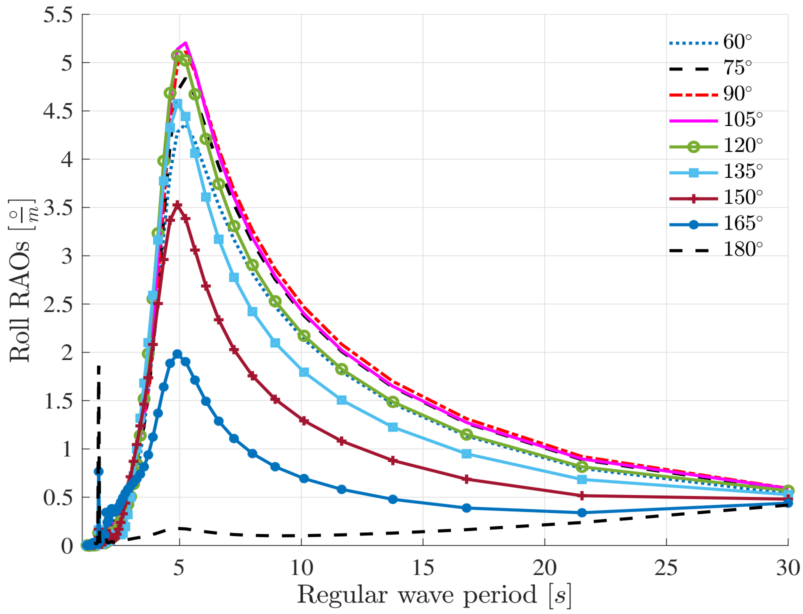

(a) Roll RAOs at different directions for case HAT empty.

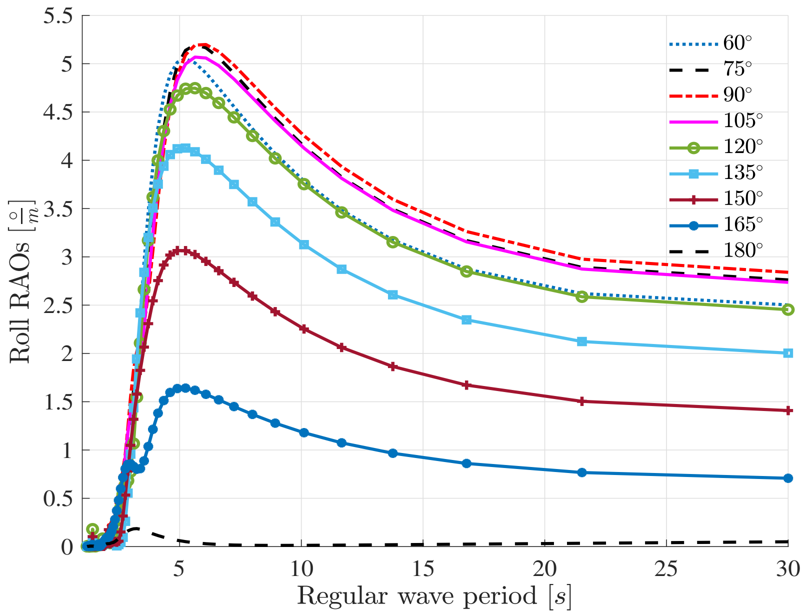

(b) Roll RAOs at different directions for case LAT empty.

Figure B.6: Visualization of roll response for different load cases at $60^\circ \rightarrow 180^\circ$ waves angles.

B.2 Forces and moments

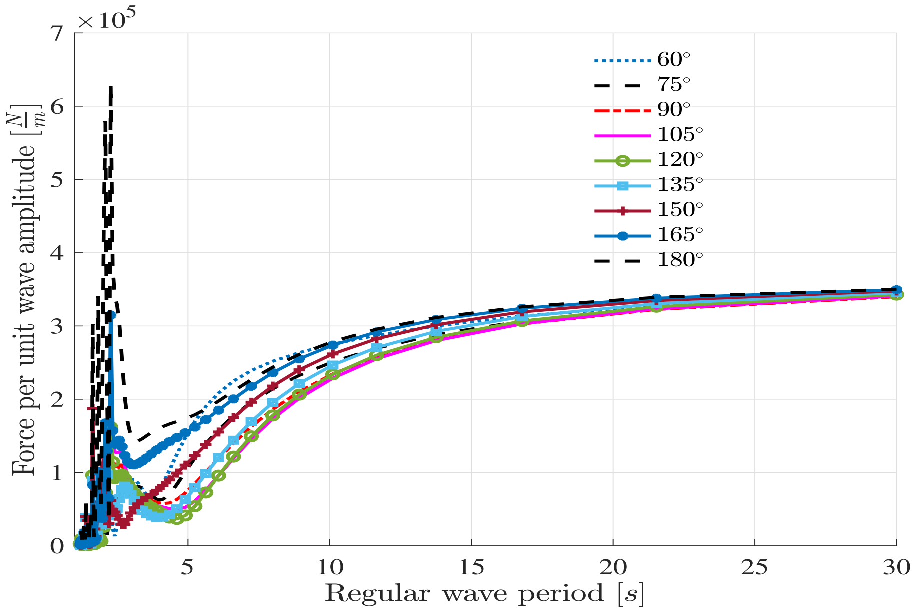

(a) Incident and diffracting surge force at different wave directions and periods for the HAT full case.

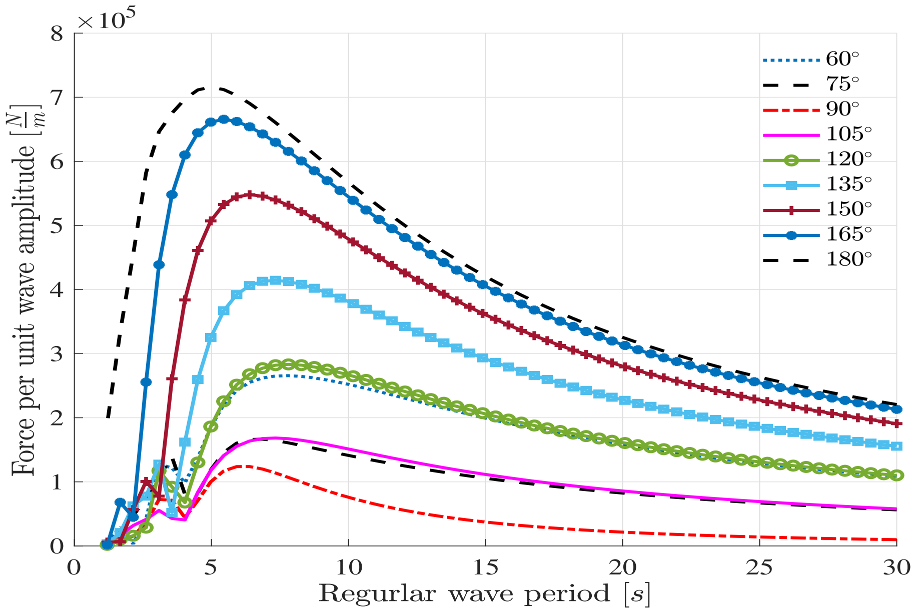

(b) Incident and diffracting surge force at different wave directions and periods for LAT full case.

Figure B.7: Visualization of incident and diffracting surge force at different wave directions, periods and cases.

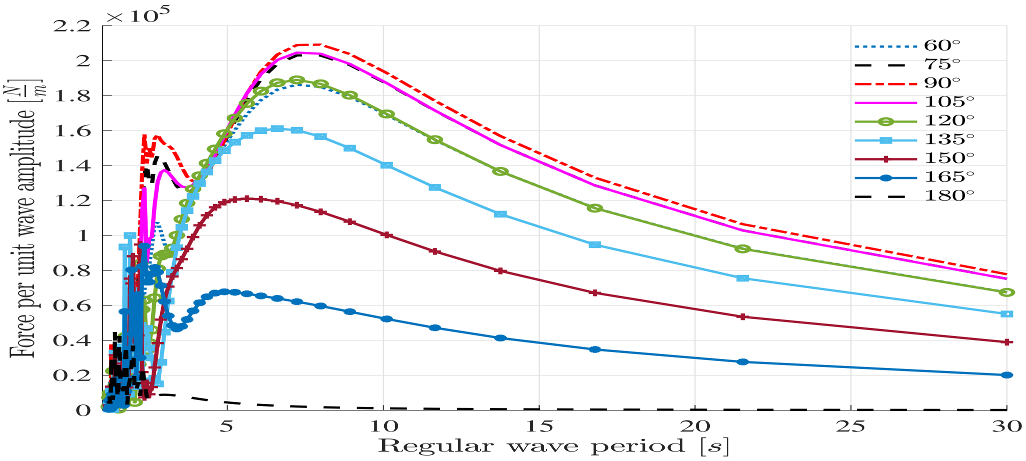

(a) Incident and diffracting sway force at different wave directions and periods for the HAT full case.

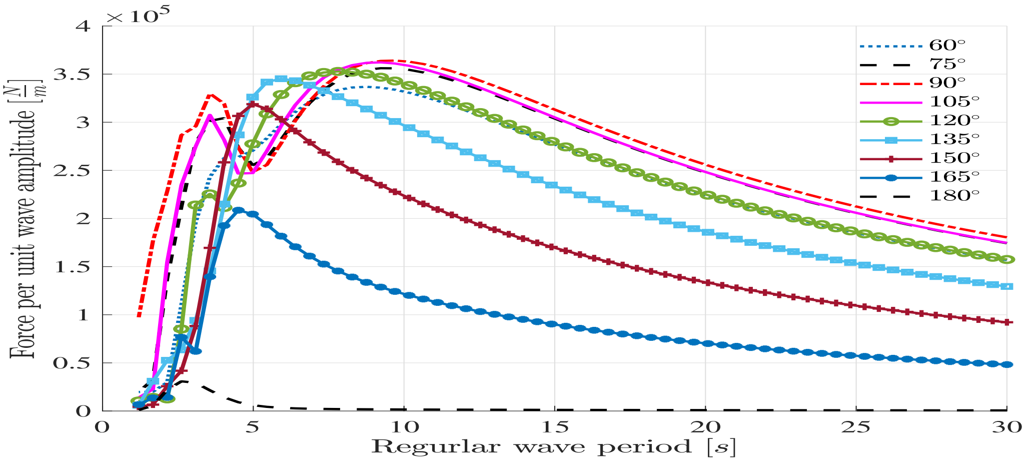

(b) Incident and diffracting sway force at different wave directions and periods for LAT full case.

Figure B.8: Visualization of incident and diffracting sway force at different wave directions, periods and cases.

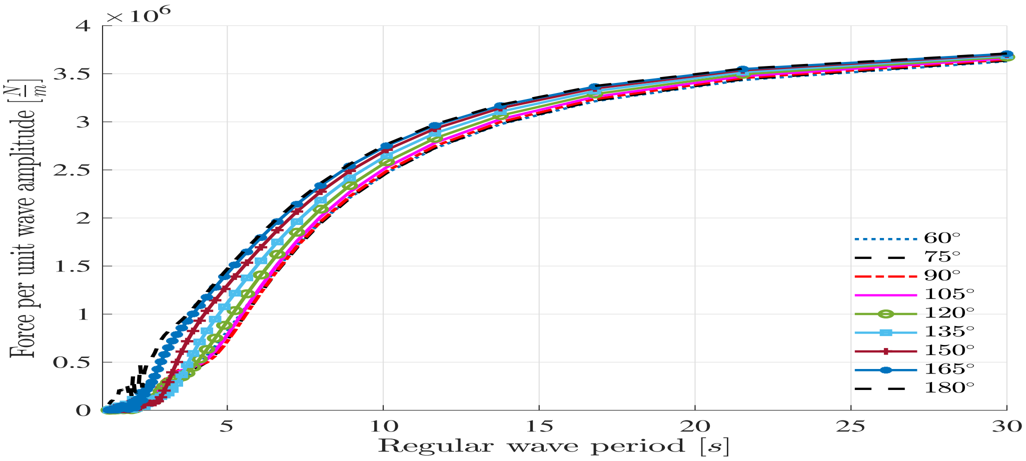

(a) Incident and diffracting heave force at different wave directions and periods for the HAT full case.

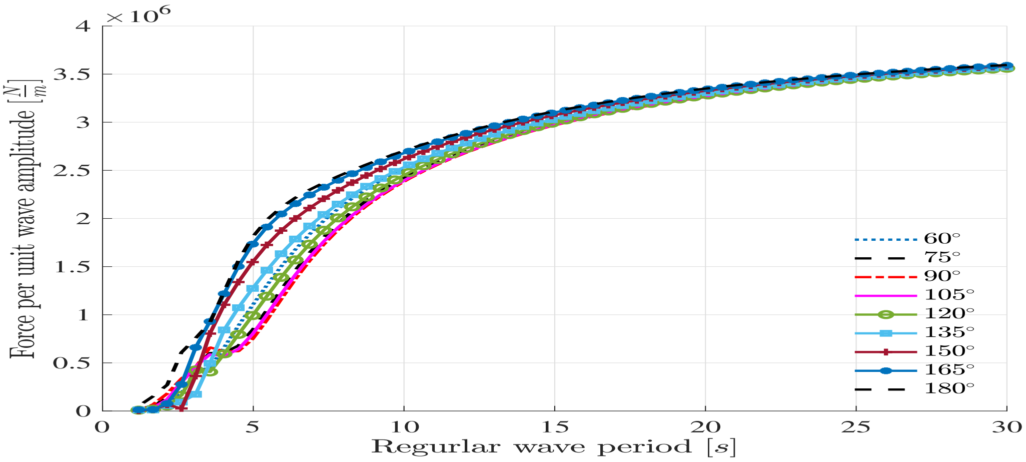

(b) Incident and diffracting heave force at different wave directions and periods for LAT full case.

Figure B.9: Visualization of incident and diffracting heave force at different wave directions, periods and cases.

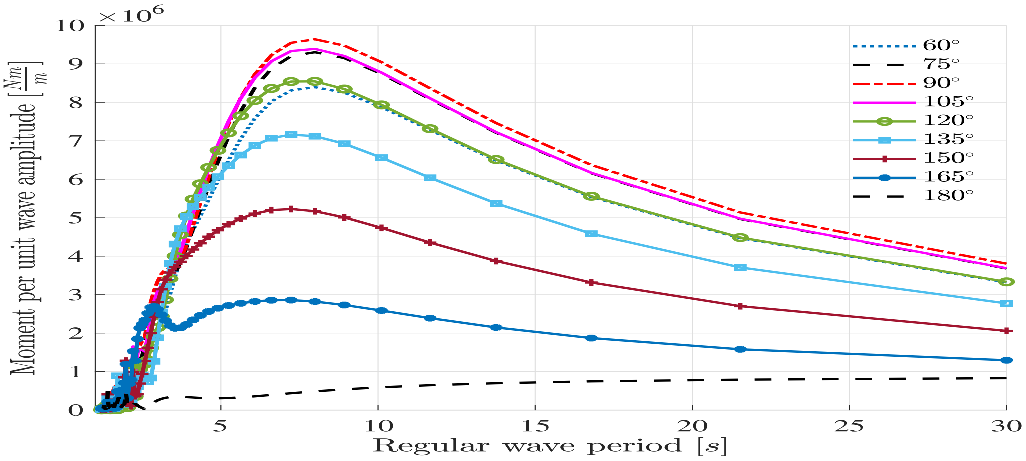

(a) Incident and diffracting roll moment at different wave directions and periods for the HAT full case.

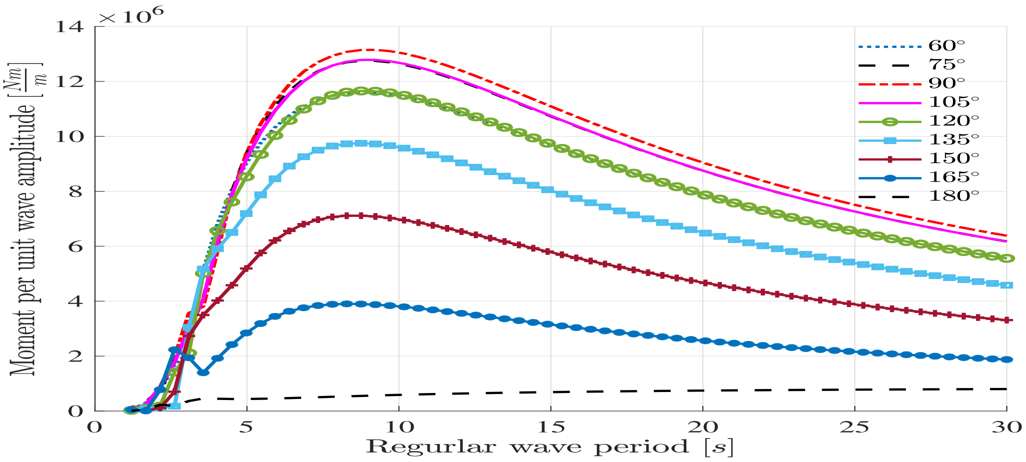

(b) Incident and diffracting roll moment at different wave directions and periods for LAT full case.

Figure B.10: Visualization of incident and diffracting roll moment at different wave directions, periods and cases.

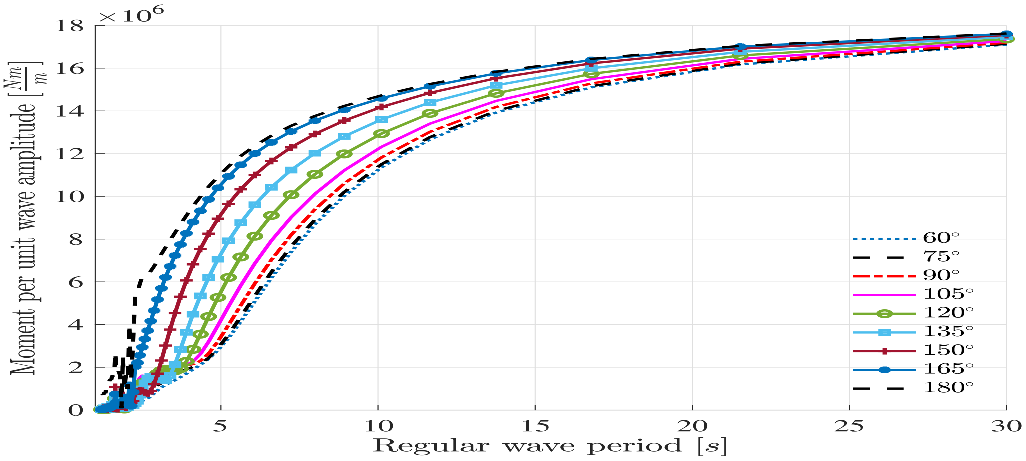

(a) Incident and diffracting pitch moment at different wave directions and periods for the HAT full case.

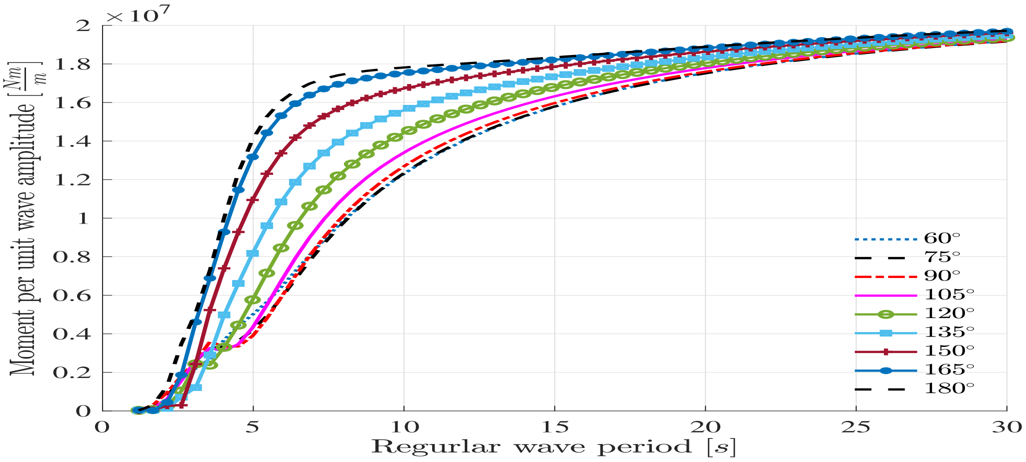

(b) Incident and diffracting pitch moment at different wave directions and periods for LAT full case.

Figure B.11: Visualization of incident and diffracting pitch moment at different wave directions, periods and cases.

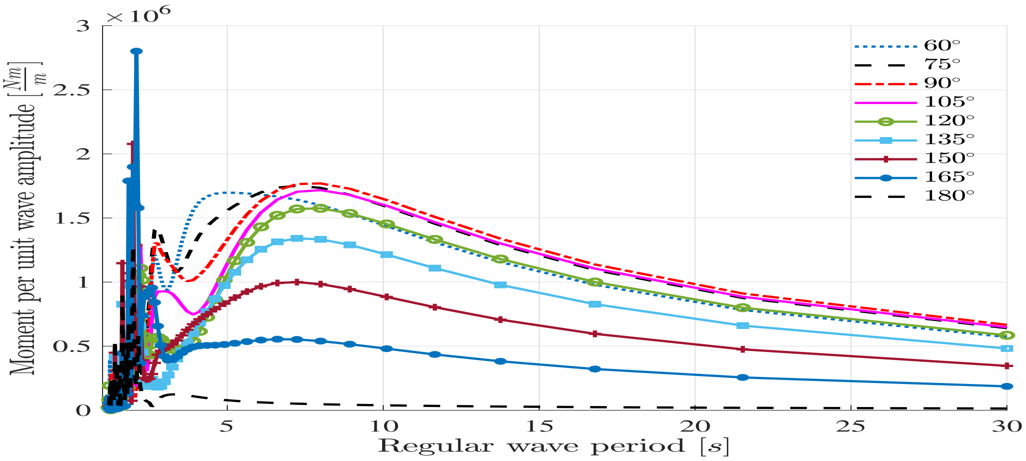

(a) [Incident and diffracting yaw moment at different wave directions and periods for LAT full case.

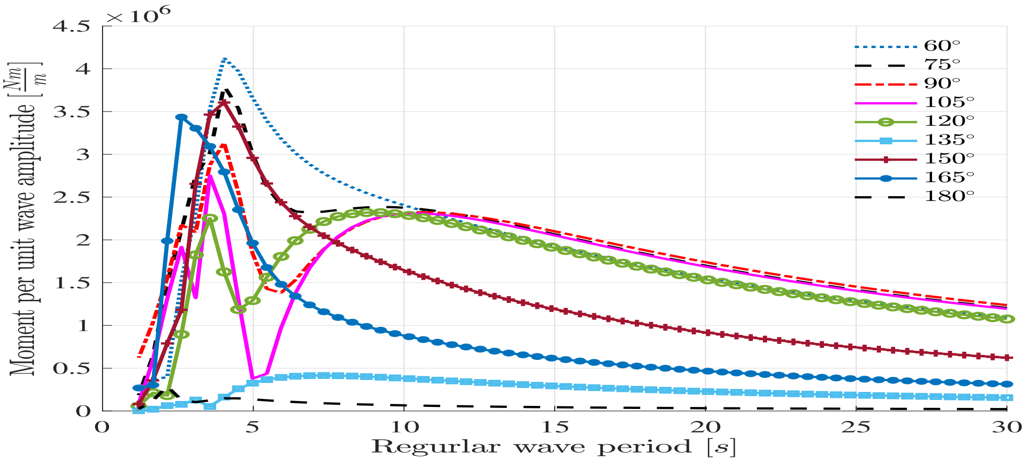

(b) Incident and diffracting yaw moment at different wave directions and periods for LAT full case.

Figure B.12: Visualization of incident and diffracting yaw moment at different wave directions, periods and cases.

Department of Mechanics and Maritime Sciences
CHALMERS UNIVERSITY OF TECHNOLOGY
Gothenburg, Sweden
www.chalmers.se

CHALMERS
UNIVERSITY OF TECHNOLOGY